Noise Mitigation of a Jet using Localized Arc Filament Plasma Actuators: Effect of Shielding Ring Groove on Control Authority of Actuators

A THESIS

Presented in Partial Fulfillment of the Requirements
for Graduation with Distinction in Mechanical
Engineering at The Ohio State University

By
Casey B. Hahn

The Ohio State University
April 2010

Examination Committee:

Dr. Mo Samimy, Advisor

Dr. Charles Haldeman

ABSTRACT

Localized arc filament plasma actuators (LAFPAs) are used at The Gas Dynamics and Turbulence Laboratory (GDTL) for the purpose of controlling the downstream development of a 1-inch exit diameter jet. The lab has the capability to study both subsonic and supersonic jets with a primary goal being the mitigation of noise emitted by a jet. However, the mechanism by which the actuators are capable of perturbing the instabilities of the jet is unclear. It has been proposed that the ring groove, initially added to shield the plasma arcs from the high-speed jet flow, of the nozzle extension that houses the actuators is crucial for effective actuation. To study this possibility a new nozzle extension, which relocates the electrodes to the nozzle extension face and deletes the ring groove, is used. A comparison of the acoustic results of a traditional extension with a ring groove and the new nozzle extension without the ring groove is used to determine the effect of the ring groove. The results show that the same general trends and levels of noise attenuation and amplification are achieved with either extension. Thus, it is concluded that the ring groove is not essential for effective actuation.

ACKNOWLEDGEMENTS

I would like to thank Dr. Mo Samimy for allowing me the opportunity to perform research at his lab. He was very helpful in introducing me to many difficult topics of fluid dynamics and aeroacoustics. I would also like to thank Martin Kearney-Fischer for his assistance throughout the past year. He trained me on the finer details of the science involved in my research and the many logistics of laboratory research.

TABLE OF CONTENTS

LIST OF FIGURES

CHAPTER 1: Introduction

Since the introduction of jet engines for use in aircraft propulsion, jet noise has been an unwanted byproduct with several negative effects on both the aeronautics industry and the public sector. As human populations increase, established airports and military airfields are continually being encroached upon while the number of flights into and out of these airports continues to rise. Furthermore, military jet engines are becoming noisier as their performance increases. As a result, noise regulations have been implemented, and many airports have had to limit flight paths and scheduling, establish curfews, and introduce surcharges. Additionally, the health of personnel who work in close proximity to jet engines, for example officers on an aircraft carrier, has become a major concern and cost.

The noise emitted from an aircraft is a combination of several different sound sources including the noise from the internals of the engines, aerodynamic noise from air rushing over the aircraft, and the jet noise of the high-speed engine exhaust mixing with the ambient air. Jet noise is the dominant source during times when noise pollution is of largest concern: during take-off and landing. Thus, in order to greatly reduce a jet engine's emitted noise, a method is required to control the jet flow downstream of the nozzle exit in such a way that a significant amount of noise is attenuated. These methods of control are divided into two categories: passive and active.

Passive controllers are the more developed technology in that they currently are used on production aircraft. The most recent example of the use of such controllers is on the by-pass nozzle of Boeing's highly anticipated aircraft, the 787 Dreamliner (Figure 1-1). Passive controllers consist of some type of geometric modification to the exit plane of the nozzle; examples include chevrons [Figure 1-1], tabs or lobbed nozzles. They have proven successful in

reducing jet noise [1] and are simple and relatively maintenance free. Still, passive controllers are inherently of fixed geometry and must be designed for a compromise of many flight conditions. Furthermore, the means in which they work require them to protrude into the jet flow reducing the performance and efficiency of the jet engine [2]. Thus, there is a need for an active controller that can operate at many different flight conditions and can be put into a neutral or off position when noise mitigation is not particularly desired.

Figure 1-1: Use of chevrons on the Boeing 787 [3].

All active flow controllers work under the same principle: additional energy in some form (e.g. heat, momentum, sound) is added to the jet for the purpose of altering the flow. Methods include acoustic drivers which use sound pressure waves to influence the flow [4]; fluidic injection using micro-jets that interact with the shear layer of a jet [5]; and, the category in which the technology discussed in this paper falls, the use of plasma as a heat and/or pressure

wave source [6-7]. Many active methods have proven successful in controlling low-speed, low Reynolds number flows. Such experiments have shed light on some of the underlying physics of jet flows and their control. However, to be applicable to real world flows of much higher Reynolds numbers, Mach numbers, turbulence intensity and momentum, actuators capable of high frequencies and high amplitudes are necessary. A technology that satisfies these conditions and has been developed and used in the jet experiments at the Gas Dynamics and Turbulence Lab (GDTL) at The Ohio State University are Localized Arc Filament Plasma Actuators (LAFPAs).

A single LAFPA consists of two tungsten electrodes at a distance of a few mm from each other and excited with several thousand volts of electricity. As the voltage reaches a critical value, the air in the gap between the two electrode tips is ionized, and a plasma arc filament forms. Figure 1-2 shows a demonstration of the plasma arcs created by LAFPAs[1]. Prior to the experiments discussed in this paper, the electrode tips have been recessed in a ring groove along the inside surface of the nozzle extension located 1 mm upstream of the nozzle extension exit. The addition of the groove is to shield the plasma from the high-speed flow that passes through the nozzle. Early experiments using extensions without a groove revealed that the plasma was convected downstream by modest flow speeds to the point where arc formation became unsustainable when sitting on the inside surface of the nozzle.

However, recent 2-D computational simulations [8] have modeled the flow and groove system showing that an unintended fluidic ejection from the groove results in response to the contained arc formation within the groove. Furthermore, this ejection produces excitation of the shear layer similar to what is observed in the actual lab experiments. Though a direct correlation

[1] The location of the actuator tips shown in this image is neither that of a traditional setup of past experiments nor that of the new, final design that is discussed in detail in Chapter 4.

between this 2-D model, which is a gross simplification of the system, and the actual 3-D experiments is not accurate, this simulation has proposed a possible mechanism behind the control authority of the actuators. The goal of this research is to determine if the ring groove is indeed essential to the control authority of the actuators. In other words, will the actuators produce the same noise attenuation results if located outside the groove? By answering this question, proposed mechanisms shall by eliminated or confirmed and more light shall be shed on the fundamental physics behind the control authority of the actuators.

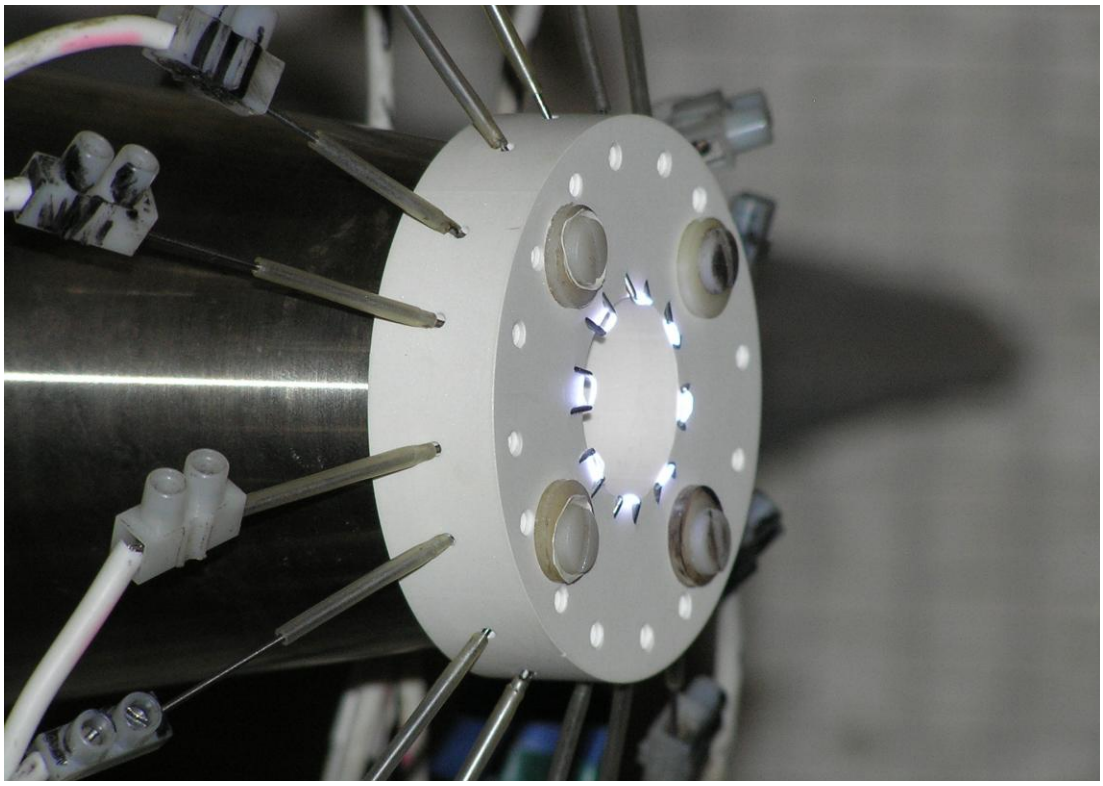

Figure 1-2: Photograph of nozzle extension assembly with firing electrodes.

CHAPTER 2: Background Information

In performing any jet flow control experiment where noise mitigation is of concern it is important to understand the physics of jet flows and the noise characteristics of the turbulent mixing of the jet. The following is an introduction to these topics.

2.1. Planar and Jet Shear Layer Instabilities

Planar shear layers such as those created by two flows of different velocities passing over opposite sides of a splitter plate have been studied for several decades. It has been discovered that the shear layer acts as an amplifier over a wide range of perturbation frequencies. This frequency range scales with the initial boundary layer momentum thickness, θ_0, and is represented in the dimensionless, normalized frequency termed Strouhal number, $St_\theta = f\,\theta_0/U$, where f is the frequency and U is the characteristic velocity of the flow. For a naturally occurring shear layer (no artificial perturbations), the frequency with the maximum growth is $St_\theta \approx 0.012$ [9]. Still, the instabilities of a natural shear layer are relatively random so the occurrence of large-scale structures will be neither spatially nor temporally coherent with merging locations varying in downstream location [7]. If perturbations are introduced, it has been found that a frequency of $St_\theta \approx 0.017$ provides the most rapid growth [10]. Exciting the jet near this frequency often produces large-scale structures which are more organized and coherent [11].

A jet can be thought of as a planar shear layer wrapped around the circumference of a nozzle. Thus, the instability mentioned above is still present in a jet shear layer and is believed to be a very important contributor to the far-field noise emitted [12]. However, there is a second instability present in a jet that is due to this fact that the shear layer is wrapped around itself. As the shear layer grows with downstream distance there is a region at which the shear layer

converges upon itself. This location is termed the end of the jet potential core and is the region where the centerline jet velocity begins to decay. The interaction of the turbulent structures from each side of the shear layer at this centerline location is nonlinear and contributes greatly to far-field noise [2]. Many researchers have studied this instability [10, 13], called the jet preferred mode or jet column mode instability, and have found that the characteristic frequency scales with the nozzle exit diameter: $St_D = fD/U_j$, where f is the frequency, D is the nozzle exit diameter and U_j is the jet exit velocity. It has been found that the natural jet preferred mode instability frequency, depending on the facility and the measurement techniques used, ranges between St_D = 0.2 and 0.6 [13] but usually is around 0.3 [11].

A third and final instability is one inherent in an axisymmetric jet. The azimuthal symmetry of an axisymmetric jet provides an additional degree of freedom in the development of the jet plume [2]. It is common to analyze the azimuthal development by Fourier decomposing individual components of the flow into what are called azimuthal modes. These azimuthal modes compete for energy and downstream amplification [7] and have been shown to scale with the ratio of nozzle exit diameter and boundary layer momentum thickness (D/θ_0) [7]. Furthermore, studies have shown that very thin shear layers ($D/\theta_0 >> 1$) will amplify many azimuthal modes [14].

2.2. Noise Emission of a Jet

The dynamics of the structures generating the far-field noise in a jet are very complicated. Dynamics of a continuum of turbulence scales from large to small emit various frequencies of noise with varying directivities. Nevertheless, jet noise has been studied for decades, and general trends have been established. All these trends are dependent on the scale of the turbulence. As stated previously, large-scale turbulence or structures interact most violently

at the end of the potential core where the two sides of the shear layer converge along the jet centerline. It has been found that this turbulent mixing of large-scale structures generates high levels of noise that dominates the noise from the small-scale turbulence of the flow [15]. However, large-scale structures have also been found to have directivity to their emission; the preferred angles for the emission by large-scale structures are those around 30° [16]. Thus, at polar angles near 90°, the influence of large-scale structures is significantly reduced and, thus, small-scale turbulence emits the majority of the noise [2].

CHAPTER 3: Experimental Facility and Techniques

3.1. Experimental Facility

All experiments were run at the Gas Dynamics and Turbulence Laboratory (GDTL) at The Ohio State University. The facility supports jets of 2.54 cm (1 in) in exit diameter at velocities ranging from subsonic to Mach 2.0. Experiments presented in this paper were conducted using an axisymmetric Mach 0.9 nozzle. Air for the jets is compressed using three 5-stage reciprocating compressors then dried, filtered and stored in two cylindrical tanks together with a volume of 43 m^3 (1500 ft^3) and a maximum pressure of 16 MPa (2300 psi). The compressed air is fed from the tanks through an electronically controlled pressure regulating valve and delivered to a stagnation chamber where pressure and temperature are measured. From the stagnation chamber, the air is fed through a perforated plate and two mesh screens for turbulence reduction and then to the nozzle. The nozzle exhausts the air horizontally into an anechoic chamber (Figure 3-1) with the following interior dimensions: 3.1 m (122 in) in width by 3.1 m (122 in) in length by 2.7 m (106 in) in height. Various measurements can be made within the chamber to assess the flow. An array of 10 microphones allows for acoustic measurements at polar angles between 25° and 90°. Additionally, certain blocks of anechoic wedges can be removed to allow for streamwise and cross-stream flow visualization and particle image velocimetry (PIV) measurements. When these measurements are being made laser pulses are sent into the chamber through a small hole in the side wall and directed through the flow using a series of mirrors and lenses. The jet flow exits the back wall of the chamber through a bellmouth to the atmosphere outside the laboratory.

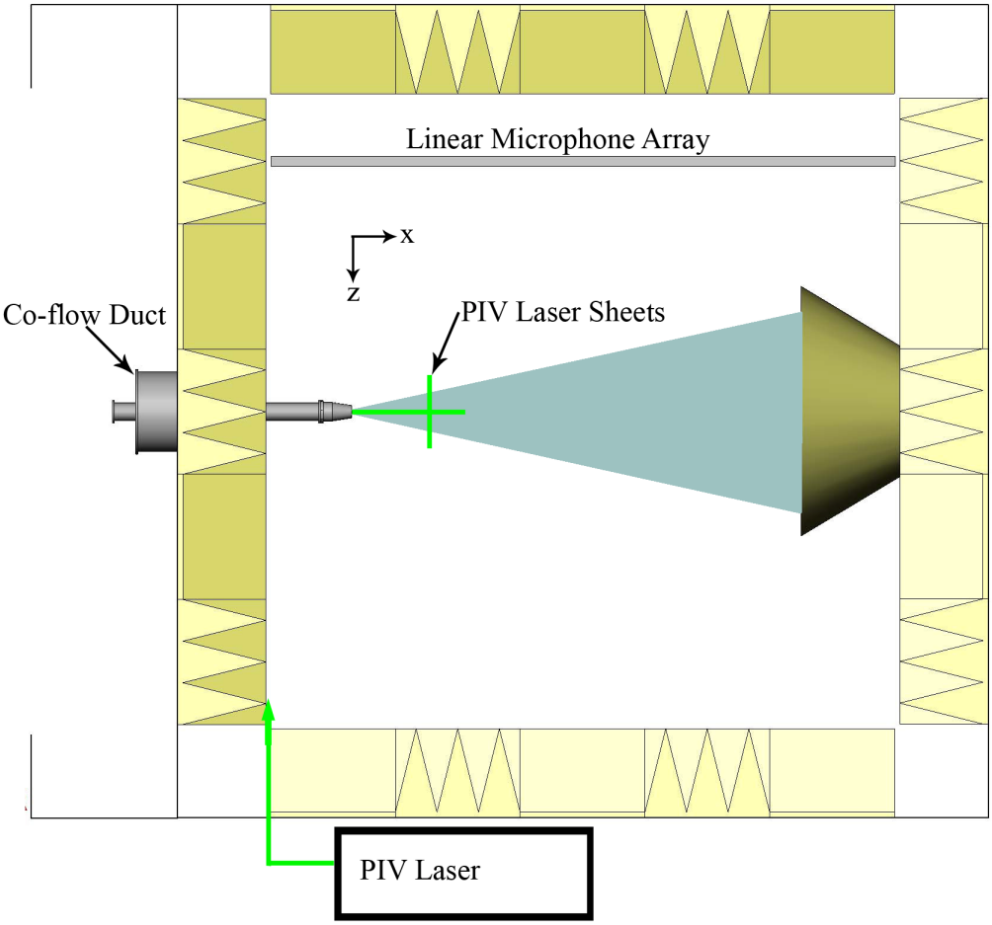

Figure 3-1: Schematic of anechoic chamber with optical access.

The facility incorporates a heating system that allows for heated jet experiments that better represent an actual jet. Total temperature ratios—the ratio between the stagnation temperature and the ambient temperature—up to 2.5 are possible. Although, as stated, a heated jet is a more accurate representation of the actual exhaust flow leaving a jet engine, including heat would add another variable to the experiments presented in this paper. In addition, LAFPAs have been shown to work similar in both cold and heated jets. Therefore, all experiments were run "cold" at a total temperature ratio near 1.0.

3.2. Localized Arc Filament Plasma Actuators and Nozzle Extensions

As previously stated, the jet flows in these experiments are controlled using localized arc filament plasma actuators (LAFPAs) that have been developed at the GDTL. The LAFPAs are located near the most receptive location of the shear layer at the nozzle exit lip. A boron nitride (ceramic) nozzle extension that houses the LAFPAs is bolted to the end of the stainless steel nozzle (Figure 3-2). Boron nitride was chosen because it is a good dielectric, has acceptable machining qualities and, most importantly, can withstand the extreme temperatures produced by the plasma arc. The traditional extension incorporates a groove along its inside surface in which the electrode tips are recessed therefore shielding them from the high-speed flow through the nozzle; the spacing between two electrodes is 4 mm center-to-center. The new extension design (detailed in Chapter 4) deletes this groove and relocates the electrode tips to the extension face. The electrode spacing is 3.5 mm center-to-center. Figure 3-3 shows a cross-section view and the dimensions (in SI units) of both extensions.

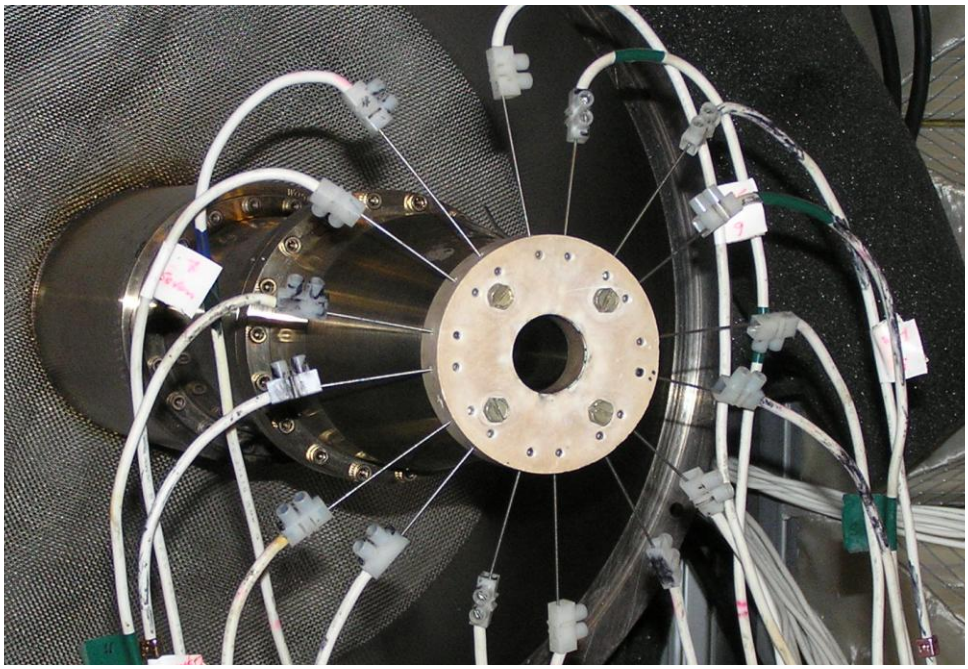

Figure 3-2: Traditional nozzle extension with LAFPA electrodes in place.

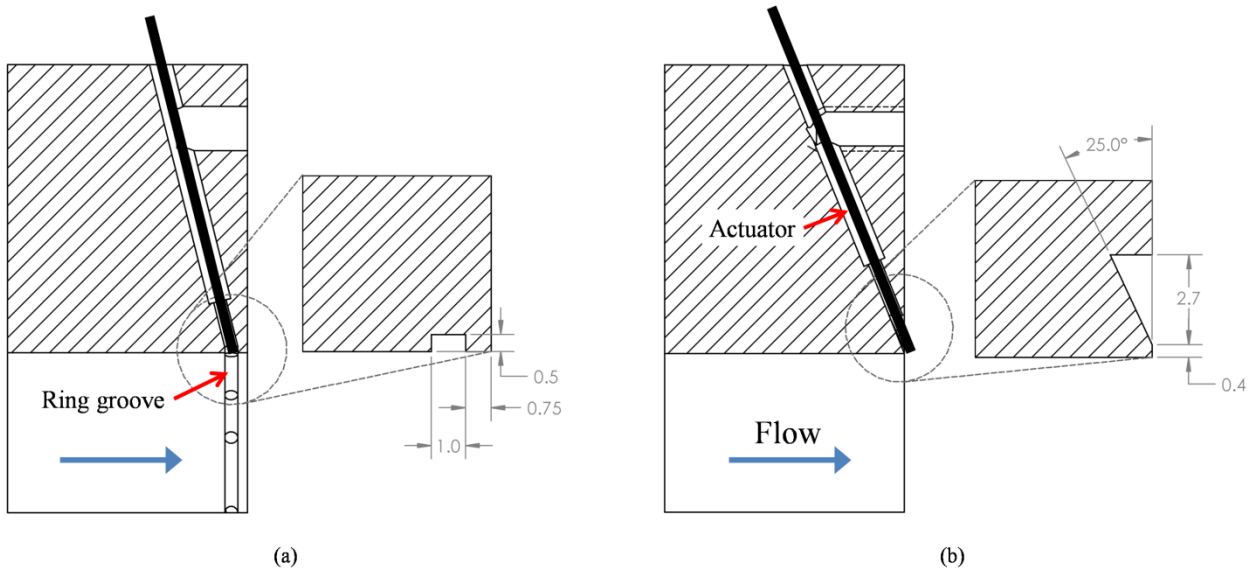

Figure 3-3: Cross-section view of (a) the traditional extension with an internal ring groove and (b) the external electrode extension with a recess on the extension face (dimensions are in mm).

The electrodes used for the actuators are 1 mm diameter tungsten rods that are commonly used for Tungsten Inert Gas (TIG) welding. A pair of electrodes composes a single actuator, and eight equally spaced actuators are used in all experiments. The plasma arcs are generated by a multi-channel, high-voltage switching circuit that was developed in-house (Figure 3-4). The generator consists of eight independent sub-circuits each consisting of an actuator connected in series with a liquid-cooled Behlke HTS 101 fast-response, high-repetition-rate, high-voltage transistor switch and two ~15 kΩ solid-body ceramic ballast resistors. Two Glassman high-voltage, high-current (10 kV, 1 A) DC power supplies provide power for the eight sub-circuits. This setup allows for independent control of each actuator with the following parameters: a large actuating frequency range of near zero to 200 kHz, high voltage pulses of up to 10 kV, short pulse rise/fall times of about 0.1 μs, and duty cycles anywhere between 0 and 50%. With 8 actuators along the perimeter of the nozzle extension the following forcing azimuthal modes (m) are possible: 0, 1, 2, 3, ±1, ±2, and ±4. Mode m = 0, or the axisymmetric mode, is the

simultaneous actuation of all 8 actuators. Modes m = 1, 2 and 3 are called the helical modes and are a discrete representation of a sinusoidal perturbation wave traveling around the inner circumference of the nozzle with wavelength, $\lambda = \pi D / n$, where πD is the circumference of the nozzle and n corresponds to the mode number. For example, mode m = 1 is the sequential operation of all 8 actuators within a single forcing period. Modes m = ±1, ±2, and ±4 are the mixed modes and are a representation of two helical modes simultaneously traveling in opposite directions.

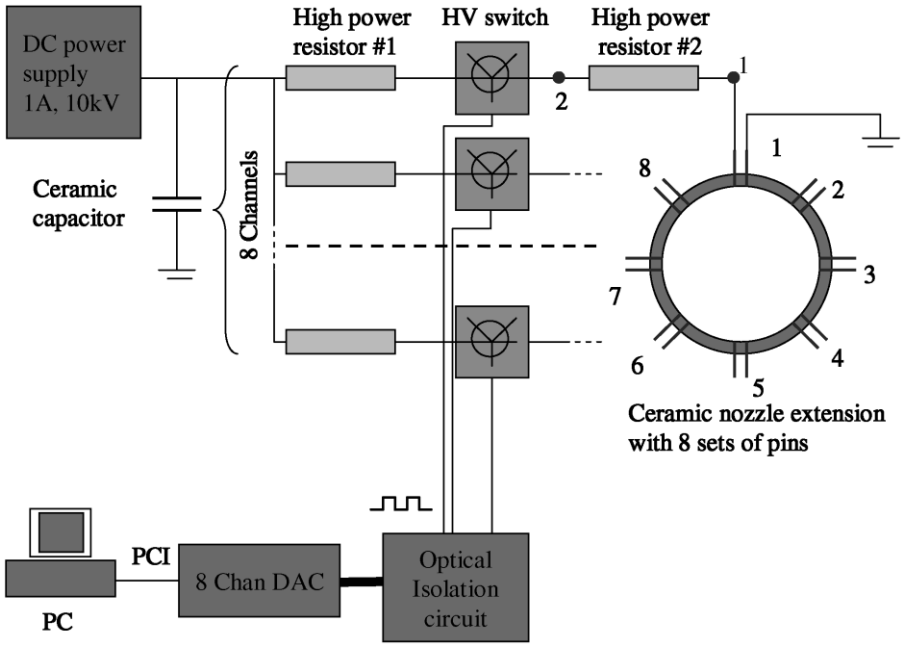

Figure 3-4: Schematic of the plasma generator used to power the actuators.

Each transistor switch is controlled by a square-wave signal generated by LabView software and a Measurement Computing Corporation PCI-2511 digital logic board. Figure 3-5 shows a typical voltage trace that is sent to a single transistor and the resulting voltage, current and power. The voltage across the gap of an electrode pair climbs as the square wave input signal switches from low to high. Once this gap voltage reaches a critical value on the order of several kilovolts, the air between the two electrodes is ionized and breakdown occurs. The

resulting plasma arc completes the electrical circuit, and the gap voltage drops to a few hundred volts while the current rises to a few hundred milliamperes. The resulting electrical power consumed is simply the product of the current and voltage traces.

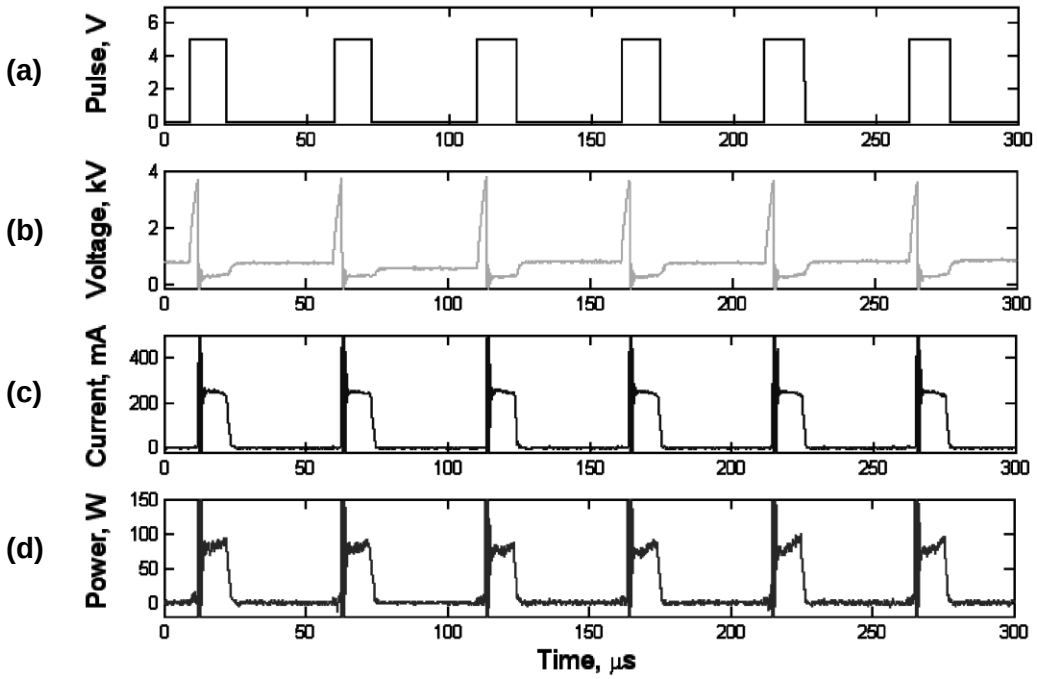

Figure 3-5: (a) The input square wave signal to a single actuator and the resulting (b) voltage, (c) current and (d) power across the electrode gap (Samimy et al. 2007b).

3.3. Data Acquisition and Processing Systems

As stated previously, far-field sound pressure level (SPL) measurements are made with a linear array of 10 microphones inside an anechoic chamber. Brüel & Kjær 4939 ¼ inch microphones with flat frequency responses up to 80 kHz are used; each is calibrated using a 114 dB, 1 kHz sine wave. The microphone signals are band-pass filtered from 20 Hz to 100 kHz using three Brüel & Kjær Nexus 2690 conditioning amplifiers with adjustable amplification rates and then acquired using two National Instruments A/D boards and LabView software. The temporal measurements are transformed into the frequency domain by applying a fast Fourier transform (FFT) algorithm. Microphone data is captured in blocks of 8192 points at a frequency

of 200 kHz giving a spectral resolution of 24.4 Hz. Any single SPL spectrum is the root mean square (RMS) of 100 blocks of data.

All acquired data is processed using multiple MATLAB functions developed in-house. The voltage traces from the microphones are converted to pressure measurements using the coefficients found during calibration for the chosen amplification rate. Measurements at each polar angle are first normalized to a similar radial distance of 80D centered about the nozzle exit—where D is the diameter of the nozzle exit—according to the fact that sound pressure level decreases as $1/r^2$ for spherical radiation, where r is the distance from the noise source (a quick rule of thumb is that SPL decreases by 6dB with each doubling of radial distance). The data is then corrected for atmospheric absorption over that distance (80D) according to the ANSI S1.26 standard. Finally, corrections for microphone orientation are made by accounting for the dependency of the microphone response on the angle-of-incidence of the incoming pressure waves. The frequency values of the recorded noise are transformed into the Strouhal number representation.

3.4. Acoustic Analysis Metrics

There is a large amount of information imbedded within the acoustic results of the jet experiments, and it must be properly condensed into several different metrics and plots for this information to be comprehensible and to provide insight into the flow dynamics. There are a vast number of possible forcing combinations and flow properties that must be analyzed. These include flow Mach number, flow temperature ratio, forcing frequency, azimuthal mode, far-field acoustic frequency and polar angle acoustic content. As stated previously this paper presents results of a Mach 0.9 jet of a temperature ratio near 1.0. Still, this leaves many variables to be analyzed, and the following is an introduction to the different methods used.

Figure 3-6 shows the spectra at a microphone angle of 30° for a typical baseline case in green and a forced case in red which shows the fundamental forcing frequency tone and several harmonics. The colored lines are the "raw" spectra while the black lines are the smoothed/detoned spectra where the fluctuations and actuator tones have been removed using a low-pass post-processing MATLAB code. The code uses a moving average filter to smooth the profiles and remove the forcing tones by substituting areas of sudden fluctuations with an average of the immediate neighboring areas. Detoning is conducted for a couple of different reasons. First, by removing the direct narrowband contribution from the actuating tones, the broadband affect of actuation can be analyzed independently. Second, preliminary results [17] have speculated that as the jet diameter is increased to a size more representative of an actual jet engine the actuator tones become less significant compared to the rest of the spectrum from the broadband mixing noise. This is due to the fact that jet noise will approximately scale with the jet area (or jet diameter to the second power) while the actuator tones will remain approximately the same.

One interesting feature of this plot is the global peak in both spectra near $St_D = 0.3$. This is in line with the jet preferred Strouhal number mentioned in Chapter 2. Thus, it can be seen that the shedding of structures at this dominant Strouhal number can be related to the emission of sound waves peaking at a similar Strouhal number. Another interesting feature is the fact that the narrowband forcing tones of the LAFPAs have an effect over the entire spectral range of the broadband jet mixing noise (in the case below it is amplification over all frequencies).

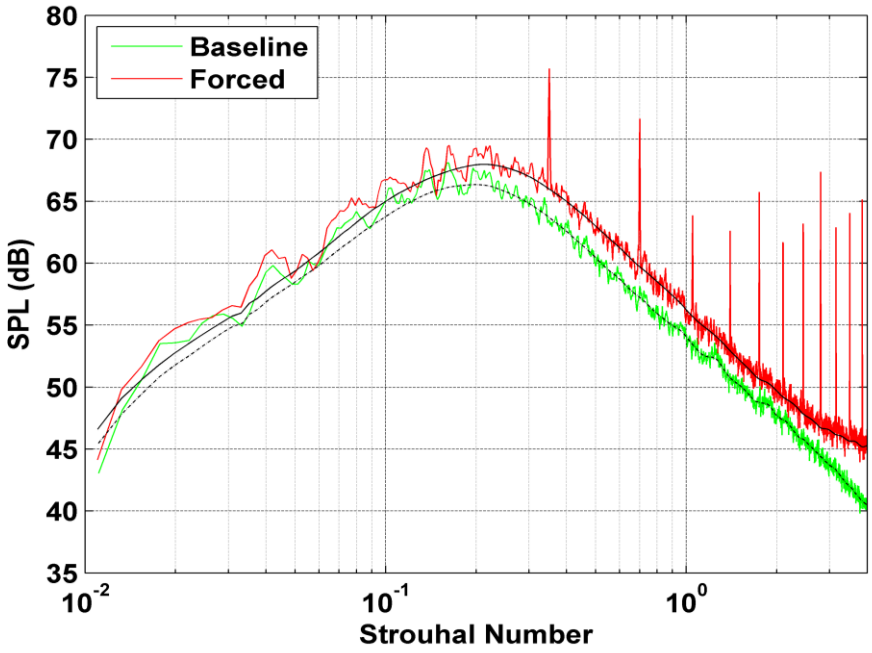

Figure 3-6: Sample spectrum showing baseline and forced case at a polar angle of 30° and St_{DF} = 0.35.

Figure 3-7 is a plot of the smoothed baseline spectra (no forcing present) of microphones at select polar angles ranging from low angles to angles near perpendicular to the jet axis. The plot shows that the noise emitted from the turbulent mixing of the jet varies greatly with orientation relative to the jet axis. It is also apparent that the ranking of polar angle from greatest to smallest noise amplitude changes with frequency. At low-to-mid frequencies, where the overall maximum amplitude occurs for all angles, the noise amplitude increases as the microphone orientation moves from perpendicular to the jet axis to smaller angles downstream of the nozzle exit. The peak amplitude at the quietest angle of 90° is ~13 dB less than the peak amplitude at the loudest angle somewhere between 25° and 30°. This trend of the greatest emission of noise being at the smaller polar angles around 30° is consistent with what was stated in Chapter 2.

At higher frequencies the ranking of polar angles by greatest noise emission changes with 50° becoming the loudest of all angles and 25° and 30°, what were the loudest angles at lower

frequencies, becoming the quietest. The explanation for this trend is fairly complicated as many factors are at play. Large-scale structures are inherently of low frequencies compared to fine-scale turbulence and, thus, are less significant in the higher frequency portion of the spectrum. Consequently, the importance of the emission by fine-scale turbulence is greater. Other variables such as where within the jet certain acoustic frequencies are generally emitted and dispersion effects from the density gradients within the flow only obscure analysis further.

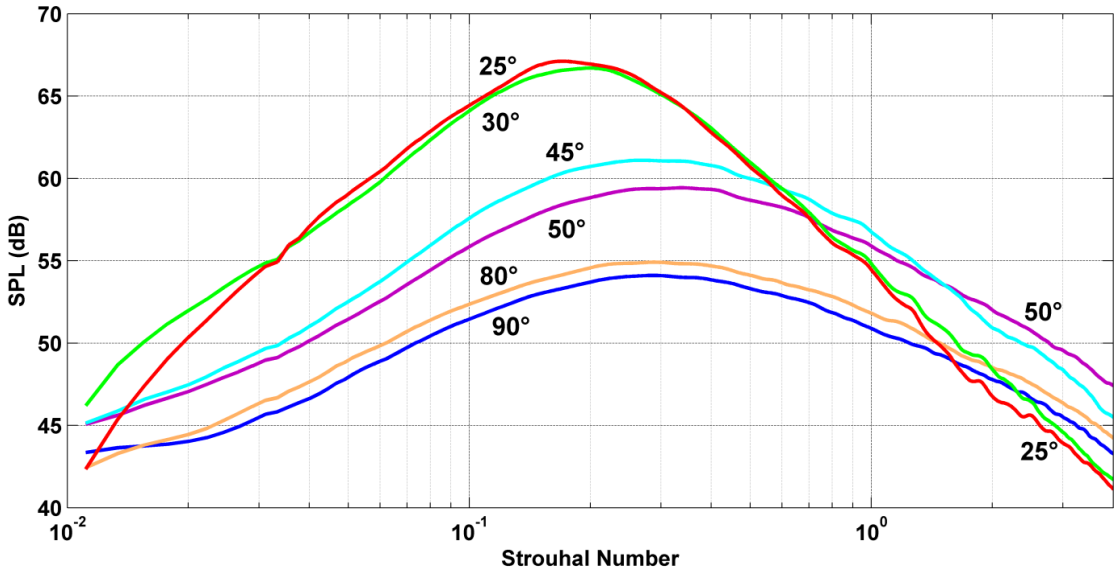

Figure 3-7: Typical smoothed baseline for multiple polar angles.

Figure 3-8 and Figure 3-9 show the effect of actuator forcing frequency on the spectra at polar angles of 30° and 90°, respectively. Again, the forced spectra without tone removal (red) show the peaks from the forcing tones. The first noticeable trend is that as forcing frequency increases the resulting spectra become quieter transitioning from amplification above the baseline across the entire spectrum to nearly zero change compared to the baseline to noise reduction for almost all frequencies of the spectrum. This trend continues to the max forcing frequency (St_{DF} ~ 3) with which was measured during this study. A second trend is that forcing at a frequency of St_{DF} = 0.35, which corresponds to the previously mentioned jet preferred

Strouhal number, creates a significant amplification in the baseline spectra. This suggests that when the actuators are firing at the jet column instability frequency the jet's natural tendency of developing coherent large-scale structures is enhanced.

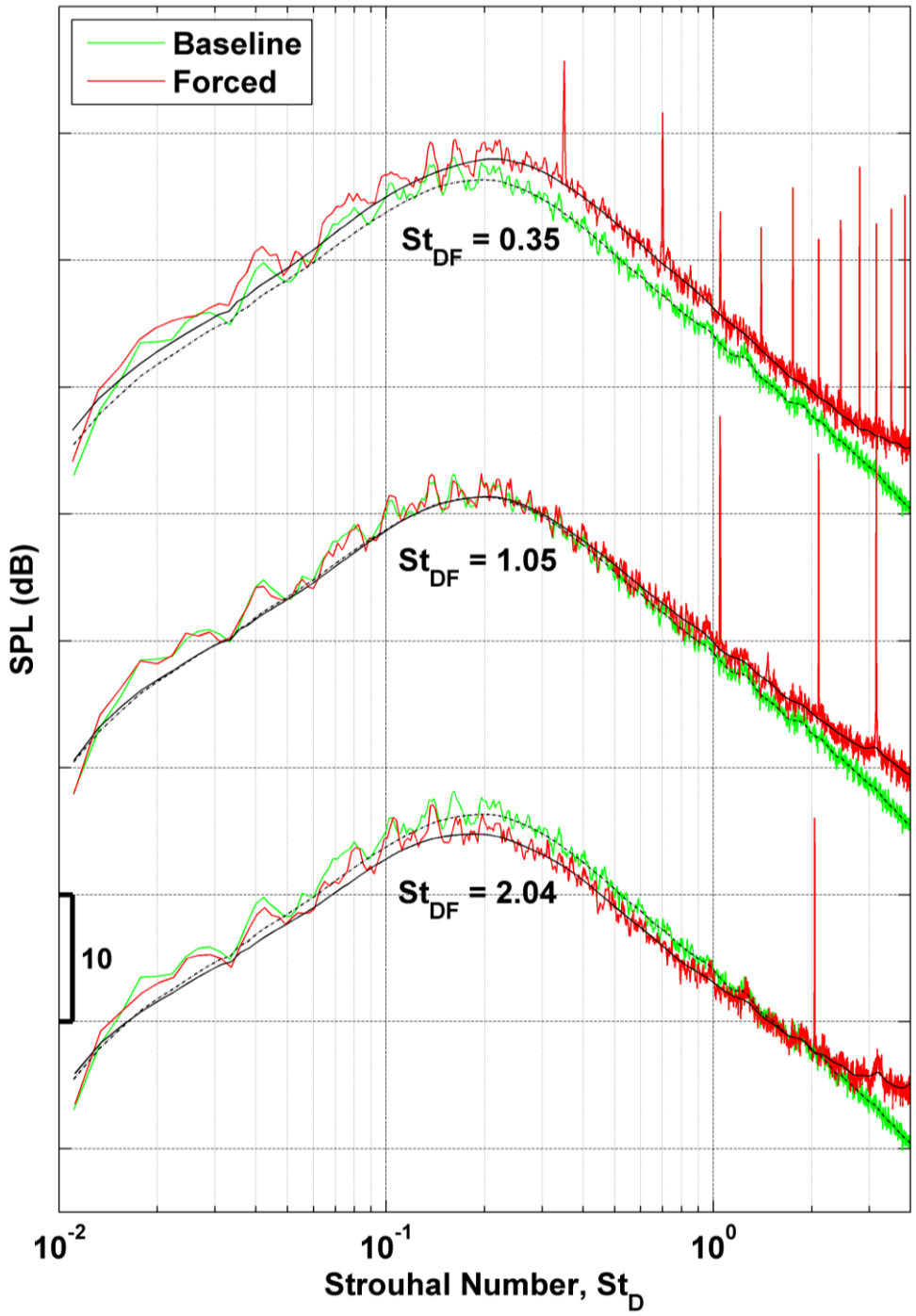

Figure 3-8: Effect of forcing frequency on typical spectra at a polar angle of 30°.

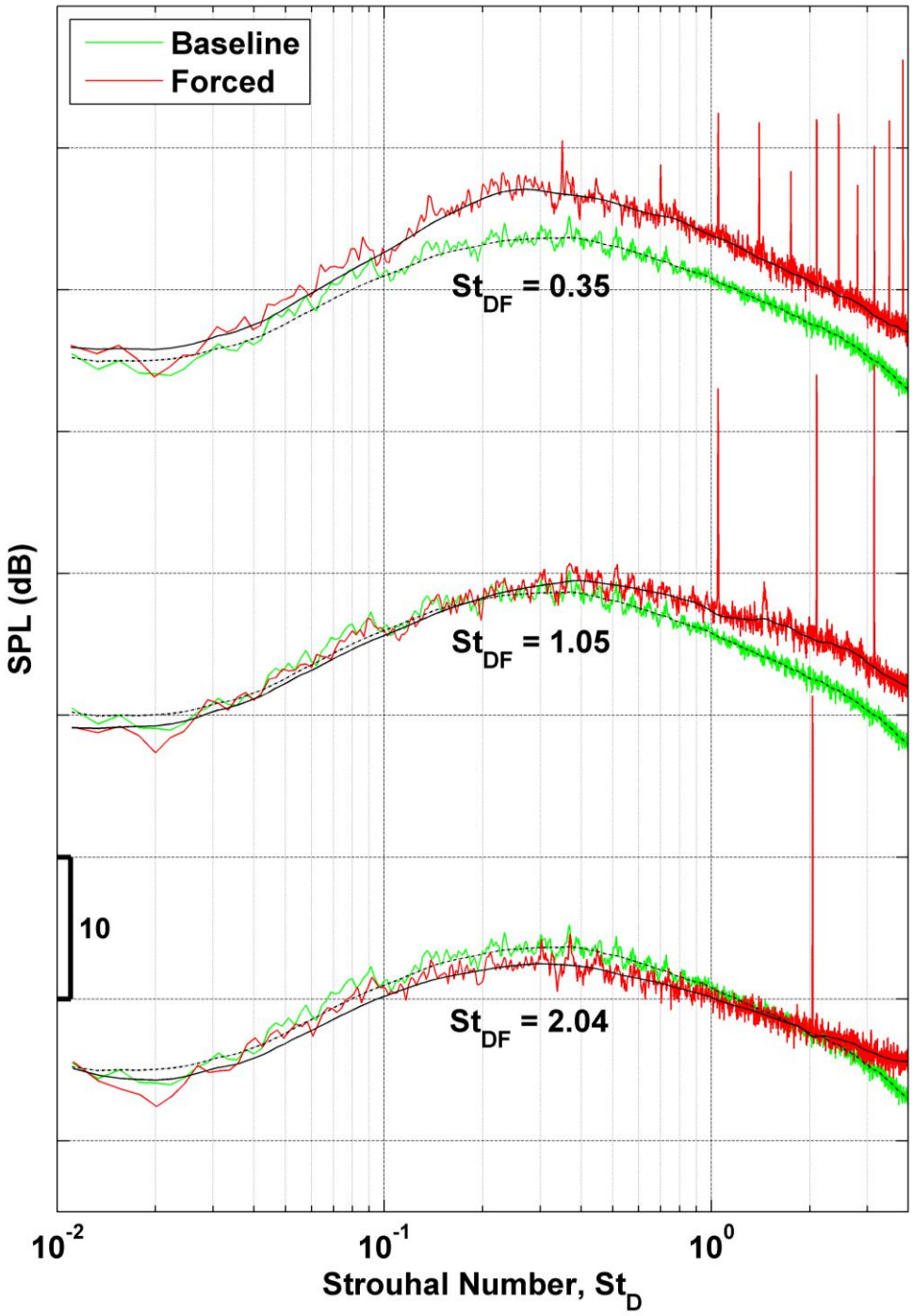

Figure 3-9: Effect of forcing frequency on typical spectra at a polar angle of 90°.

Each of the above spectra can be represented with a single quantity by integrating the SPL values over the entire frequency domain. This parameter is the overall sound pressure level

(OASPL) and is a measure of the acoustic power incident on the given microphone. The calculation is as follows:

$$OASPL = 10\log_{10}\int_{St_D=0.04}^{4} 10^{\frac{SPL(f)}{10}}\,df$$

The limits of the summation are such that the great majority of the SPL content is accounted for in any and all spectra recorded. It should be noted that the OASPL measurement for a given spectrum is equal to RMS value of the same pressure measurements in the time domain.

What is of particular interest when calculating OASPL values of the forced spectra is the change in the OASPL value for a corresponding baseline spectrum, or simply ΔOASPL. Figure 3-10 shows the ΔOASPL for the 30°, 50° and 90° microphones plotted against forcing Strouhal number for the same data shown in Figure 3-8 and Figure 3-9. In examining the spectra for St_{DF} = 0.35 in the two figures above, it appears as if the amplification at the 90° microphone is greater than that at the 30° microphone over the entire spectra. This trend is verified by the ΔOASPL values of Figure 3-10 corresponding to the same St_{DF} = 0.35[2]. Other trends that were discovered in the two figures above can also be easily observed with ΔOASPL values including the changeover from amplification to attenuation with increasing forcing Strouhal number.

[2] It should be noted that although amplification/attenuation at 90° may be greater than that at 30° for a given forcing case, the changes at 30° are much more significant because the noise energy at this polar angle is at higher absolute value.

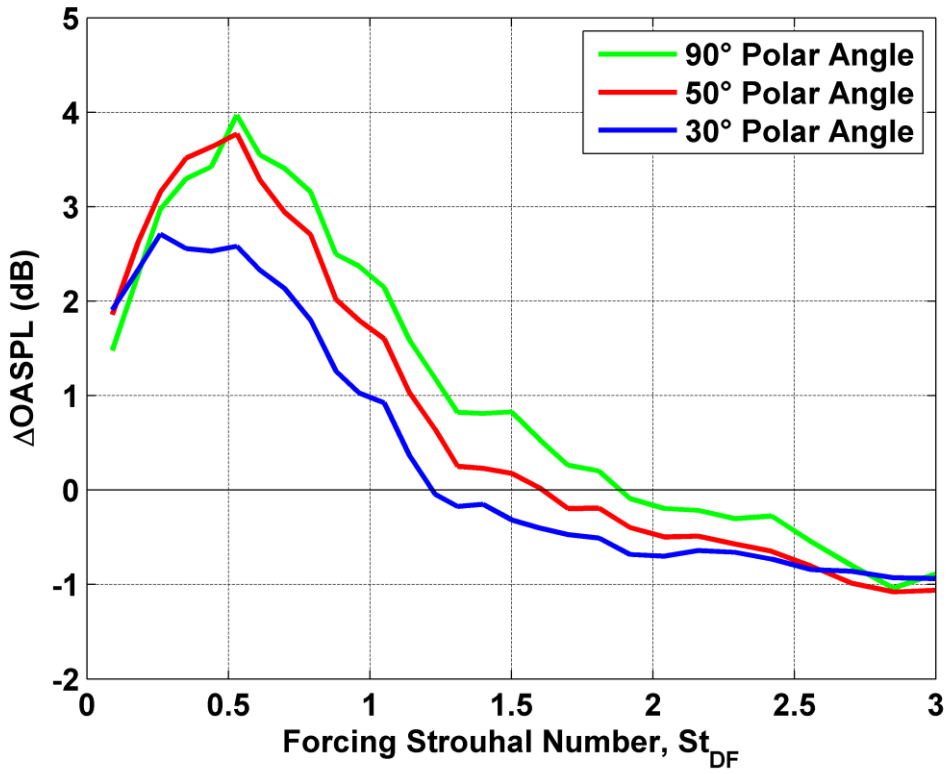

Figure 3-10: Sample ΔOASPL (dB) plot showing variation with forcing frequency for three polar angles.

An additional method of presenting ΔOASPL values is in the form of a contour plot with forcing Strouhal number in ascending order along the ordinate and polar angle in descending order along the abscissa. Figure 3-11 shows the data for the angles 30°, 50° and 90° detailed above as well as the remaining microphones at 25°, 35°, 40°, 45°, 60°, 70° and 80°. The contour lines are drawn with a resolution of 0.3 dB, and the blue and green regions designated amplification and attenuation, respectively. Plotting ΔOASPL levels in this manner gives both a quick qualitative and quantitative measurement of the effectiveness of the actuators for each azimuthal mode. Thus, ΔOASPL plots can successfully condense data while still bringing to light specific trends of the acoustic signatures of a jet flow.

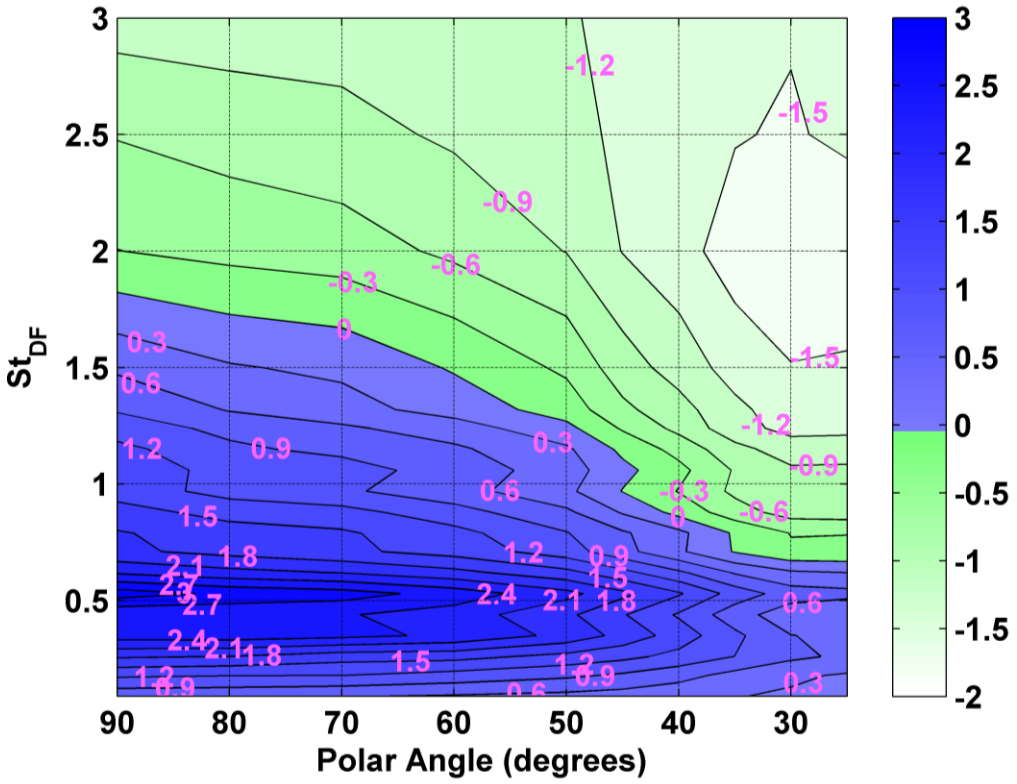

Figure 3-11: Sample contour plot of ΔOASPL (dB) values for a given azimuthal mode.

A final logical compression of the data is the calculation of the average acoustic energy (AAE) or the change in average acoustic energy (ΔAAE) if calculating changes above or below a baseline spectrum. AAE is calculated by averaging the SPL levels of all 10 microphones for a given forcing frequency and azimuthal mode and then converting these average values to decibels. Thus, it would represent the average along any horizontal line in the sample ΔOASPL plot of Figure 3-11. Compressing the data in this manner allows for all the data measured during a comprehensive acoustic experiment to be plotted on a single graph (Figure 3-12). Thus, it can reveal some of the most general trends for a specific experiment.

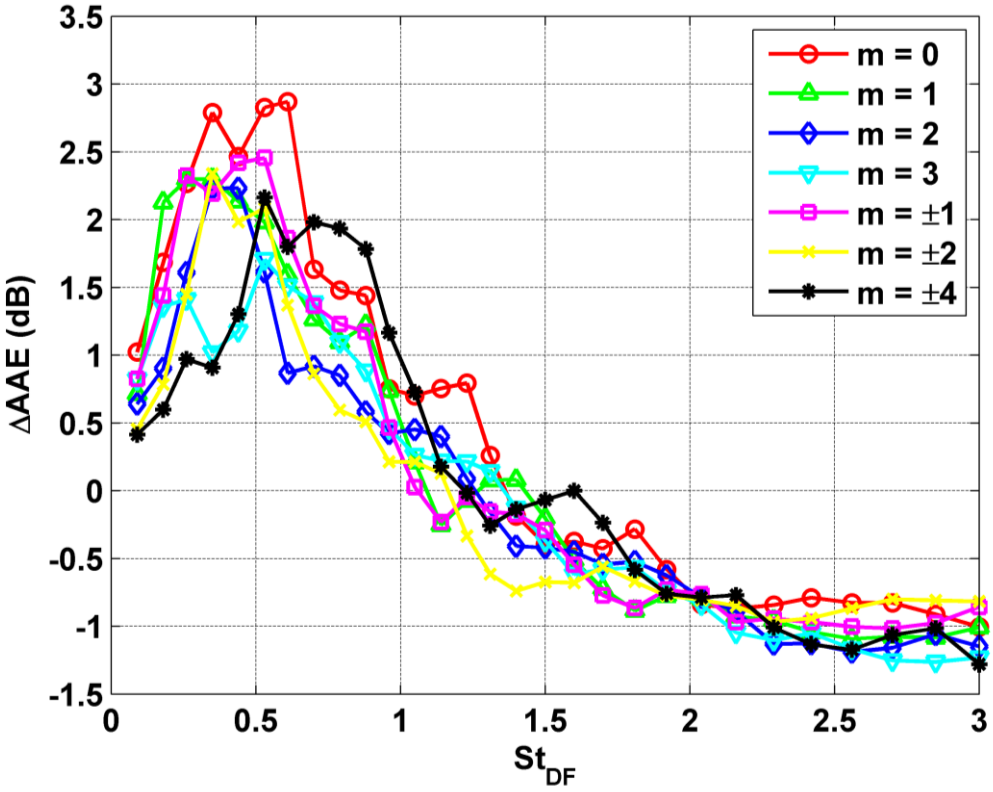

Figure 3-12: Sample plot of ΔAAE (dB) values.

CHAPTER 4: Results

As stated previously, the goal of this research is to determine to what extent the plasma shielding ring groove of the traditional nozzle extension affects the control authority of the actuators. Recent computational research has suggested that the ring groove has effects beyond simply shielding the plasma arcs; it states that from the groove a micro-jet is ejected into the boundary layer just upstream of the nozzle exit due to the thermal expansion by the localized heating of the plasma actuation. The study proposes that it is this fluidic ejection which provides perturbations to the instabilities of the shear layer and triggers the growth of the observed large-scale structures downstream of the nozzle. It has long been known that the initial perturbation by the LAFPAs is indeed a thermal one. However, because the flow is compressible and the rapid, localized heating is on the order of microseconds, compression waves are generated (Figure 4-1). Researchers at the GDTL instead believe that it is this thermal perturbation, the pressure wave perturbation, or a combination of the two which acts as the mechanism of perturbation.

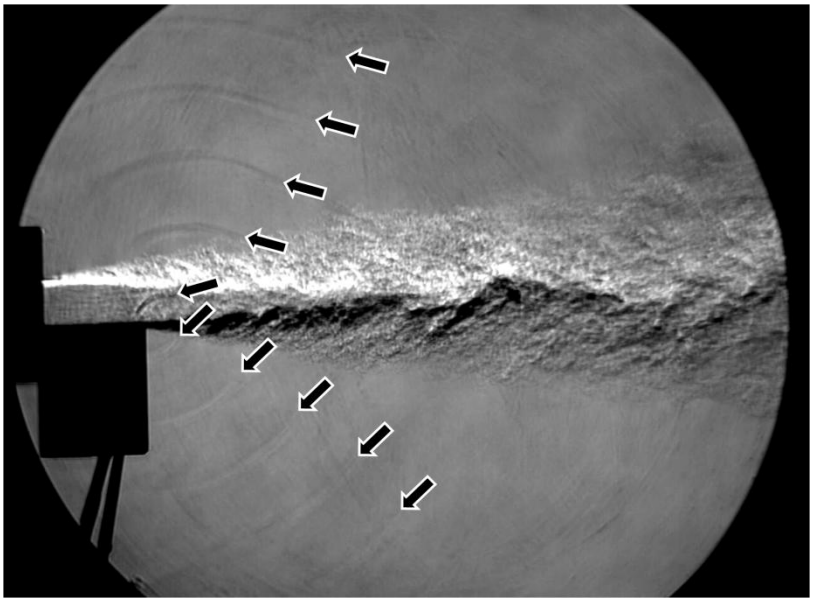

Figure 4-1: An instantaneous schlieren image showing the compression waves (indicated by arrows) generated by LAFPAs operating in a Mach 0.9 rectangular jet.

To investigate these theories it was necessary to remove the ring groove from the experiment while still retaining stable plasma arcs. If done successfully, the possibility of fluidic ejection perturbations is avoided, and the only possible perturbation is the Joule heating and/or the resulting pressure waves. Detailed analysis and comparison of acoustic measurements of both a traditional nozzle extension with a ring groove and the new design without a ring groove is used to verify whether or not the ring groove is indeed necessary for effective control by the actuators. However, before valid acoustic measurements could be recorded, troubleshooting had to be performed and modifications had to be made to the new nozzle extension design in order to achieve stable plasma arcs at speeds of Mach 0.9. The following is a description of the steps taken to arrive at the final, operational external electrode nozzle extension followed by a description and comparison of the acoustic measurements obtained with this extension and a traditional design.

4.1. External Electrode Nozzle Extension: First Attempt

The initial design for the new extension simply relocated the 16 holes for the electrodes from within the inner bore of the nozzle extension to the face of the nozzle exit (Figure 4-2). This allowed deletion of the ring groove. However, the greater exposure of the electrode tips proved to be the flaw with this initial design.

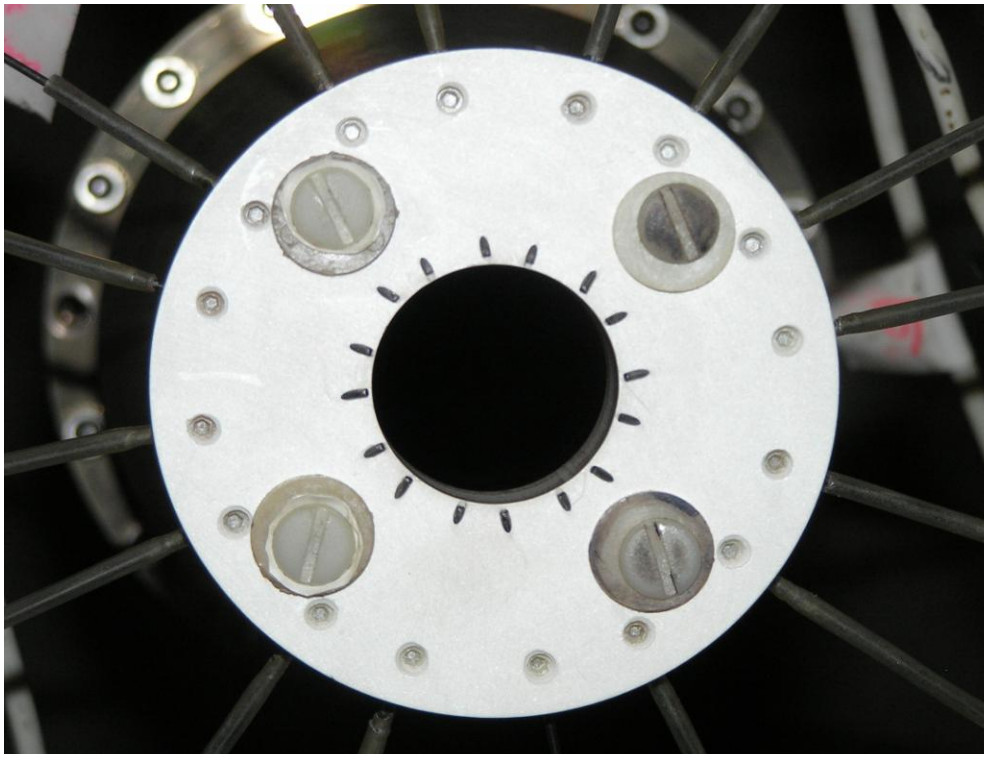

Figure 4-2: Initial design for the external electrode nozzle extension.

Initially the electrodes were positioned so that their tips were even with the flow of the nozzle. However, when attempting to run the jet at full speed (Mach 0.9) breakdown could not be consistently achieved. In an attempt to bring the tips away from the high-speed flow, the electrodes were pulled radially outward as far as possible. In spite of this, consistent operation of the actuators was not possible at speeds higher than about Mach 0.5. This was either a result of the electrodes still being too close to the high-speed jet, the velocity of the entrained air passing over the electrodes being too great, or, most probably, the spacing between electrodes now being too large for the given voltage input. Next, though counterintuitive, it was attempted to pull the electrodes inward to the point that they were protruding into the jet flow in order to bring the electrode tips closer together than when in their original orientation (Figure 4-3). In spite of now being within the high-speed jet, stable breakdown was achieved at Mach 0.9 (Figure 1-2).

However, this setup was not acceptable as the electrodes themselves were now a secondary perturbation to the flow, and any acoustic measurements would not be directly comparable to those from a traditional nozzle extension. Nevertheless, the fact that the actuators in this position were stable at the required Mach number revealed that the plasma stability is most sensitive to actuator spacing. For a fixed voltage, as electrode spacing increases the strength and resilience of the plasma arcs are greatly reduced and the effect of the flow velocity passing over the electrodes is greatly increased. Thus, in an attempt to stabilize the electrodes while in a position in which they were not protruding into the flow, the extension was modified in order to shield the actuators from the momentum of the entrained air yet without creating a groove similar to the one on the traditional extension.

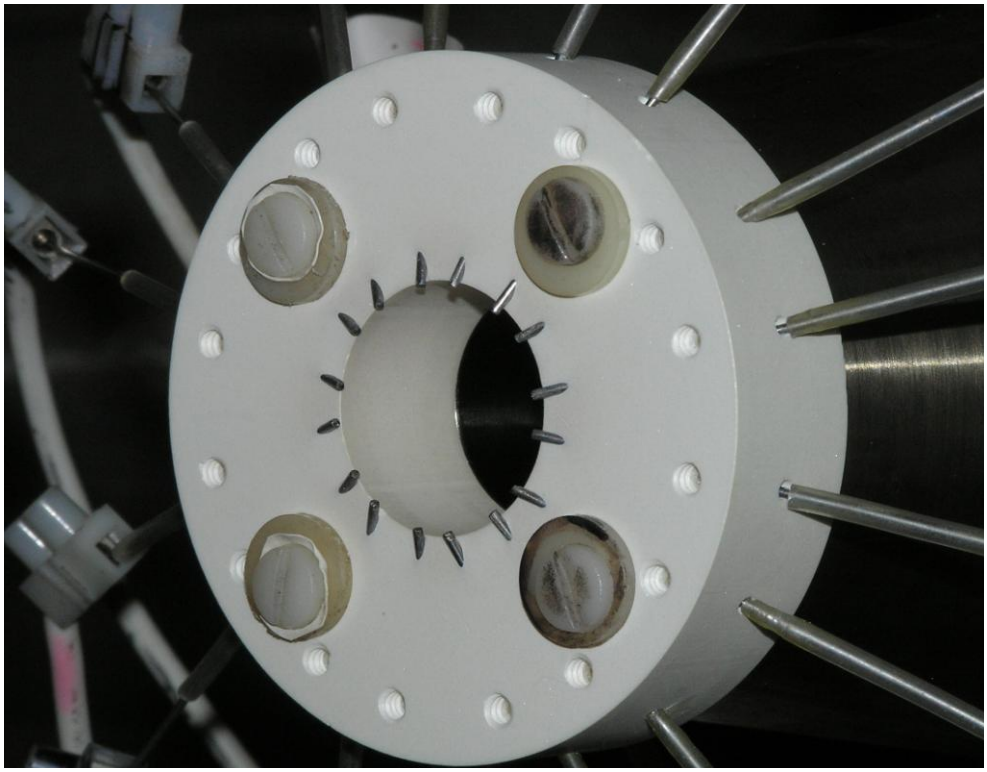

Figure 4-3: Required position of the electrodes for stable breakdown at Mach 0.9.

4.2. External Electrode Nozzle Extension: Addition of a Recess to Extension Face

In order to shield the plasma from the entrained air, a recess was machined into the nozzle extension face. However, this recess was not of simple square cross-section like the ring groove of the traditional extension for two reasons. First, a square cross-section would obstruct any direct path of the pressure waves from the actuators to the origin of the shear layer at the nozzle exit where the flow is most receptive. Second, the recess had to be shaped and sized as to satisfy the condition that it would not act as a cavity out of which fluidic ejection might occur. Thus a recess of triangular cross-section, dimensioned in Figure 3-3 and shown in Figure 4-4, was chosen to satisfy both requirements. The shape and size of the modification allow it to act more like a ledge—rather than a cavity—against which the electrode tips are positioned causing the entrained air to somewhat flow over top of the plasma.

The modification did provide stable plasma arcs at somewhat higher jet velocities, but the entrained momentum still proved to be too great at a jet speed of Mach 0.9. Thus, the last option available to obtain a working concept was to reduce the electrode spacing. Instead of incurring the large expense of having a new nozzle extension machined, it was decided to bend inward the tip of one electrode of each of the eight actuator pairs in order to reduce the center-to-center spacing from ~4.5 mm to ~3.5 mm as is shown in Figure 4-4. Because of the brittle nature of tungsten electrodes, spring steel wire of identical diameter (1 mm) was used for the bent electrode. Spring steel erodes at a much faster rate than tungsten under the conditions of the actuator experiments. Still, the spring steel electrodes endured long enough to obtain all the needed acoustic data for the new nozzle extension.

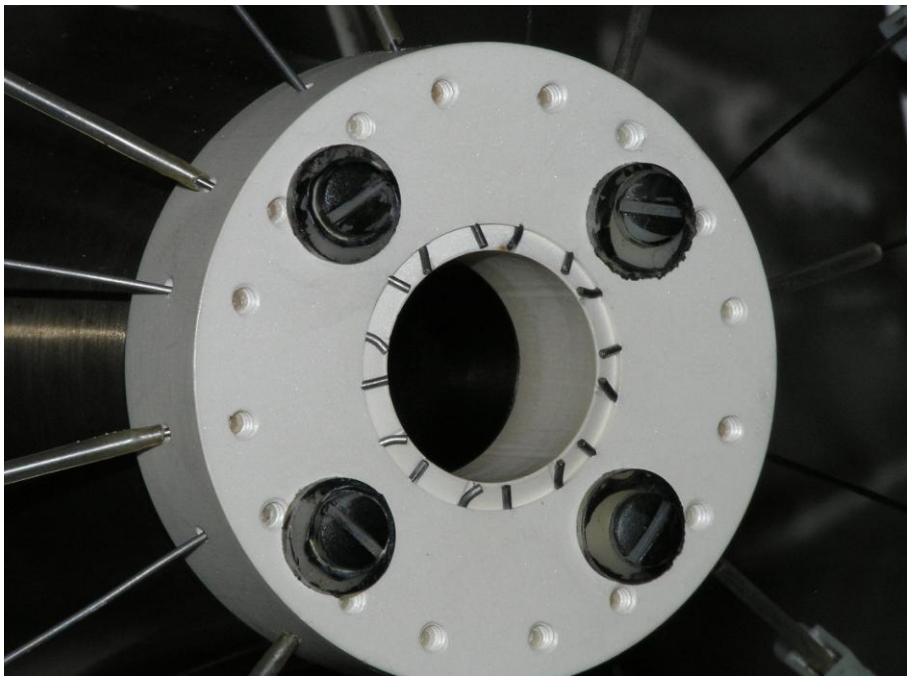

Figure 4-4: Image of the final design and setup of the new nozzle extension.

4.3. Traditional Nozzle Extension: Mode Zero Discrepancy

For the purpose of consistency, a new traditional nozzle extension was machined around the same time as the external electrode extension. This decision was made because the groove geometry erodes slowly over a few years of use. Complete acoustic data was acquired for both nozzle extensions for all possible azimuthal modes and 29 forcing Strouhal numbers between St_D = 0.01 and 3.0. Once the data for the traditional nozzle extension was processed and analyzed, it was observed that the forcing cases for mode zero exhibited some odd behavior when compared to similar data taken in previous years using older yet identical traditional extensions. Figure 4-5 compares the spectra for all polar angles for data taken using an older extension manufactured in February of 2007 and data taken using the new extension manufactured in March of 2010. It is seen that while the low-frequency content is consistent (other than small differences in overall magnitudes due to slightly different jet temperatures) the high-frequency content varies greatly. While the spectra for the older extension fall at a more-or-less constant rate at higher

frequencies, the spectra for the new extension tend to stay elevated at the highest frequencies. Furthermore, there are obvious fluctuations between every forcing tone harmonic with peaks exactly midway between each neighboring harmonic. This trend is also apparent in almost every set of spectra for the other forcing frequencies of mode zero for the new extension. Additionally, Figure 4-6 shows the ΔOASPL contour plots for mode zero for both extensions. It is obvious that the spectra for all polar angles and forcing frequencies of the new extension are elevated when compared to the respective spectra of the older extension.

It was decided to recapture all forcing frequencies for all azimuthal modes to verify whether or not the first data set did indeed contain some error. When the second round of data was processed and analyzed, the oddities described above were no longer realized. Figure 4-7 shows the spectra for all polar angles for mode m = 0 and a similar forcing Strouhal number as the plots above. It is clear that the recaptured spectra no longer contain the fluctuations at higher frequencies and agree much better with the spectra from the older extension. Furthermore, Figure 4-8 shows the ΔOASPL contour plot for mode zero for the recaptured data. Again, the data better agrees with the results of the old extension. Thus, this recaptured data proved to be satisfactory and is used in the comparison with the external electrode nozzle extension in the next section.

It is not currently known why the new nozzle extension initially exhibited odd behavior, why it was only exhibited when forcing with m = 0, or why the peaks of the fluctuations were exactly midway between neighboring harmonics of the fundamental forcing tone. However, this is not a new phenomenon as odd behavior has been noticed by other researchers at the GDTL when using a new extension for the first time; a new extension seems to have some sort of break-in period. Since the behavior of the arc is sensitive to variables like the circuit capacitance, it is

likely that exact characteristics of the circuit change slightly during the first few runs with a new extension. More research is necessary to understand this phenomenon.

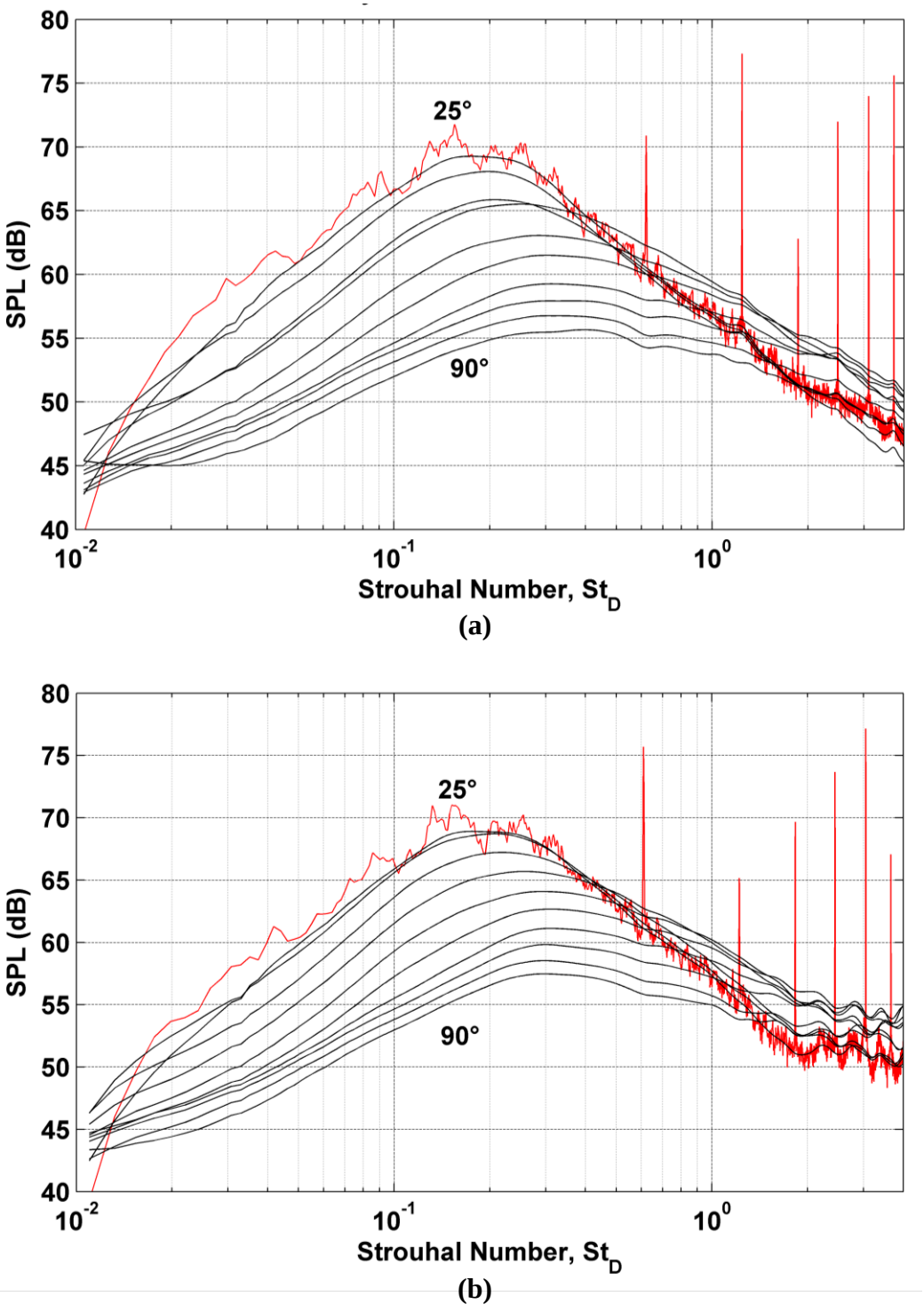

Figure 4-5: Spectra for mode m = 0 using (a) an older traditional extension, St_{DF} = 0.62, and (b) the new traditional extension, St_{DF} = 0.61 showing differences at higher frequencies.

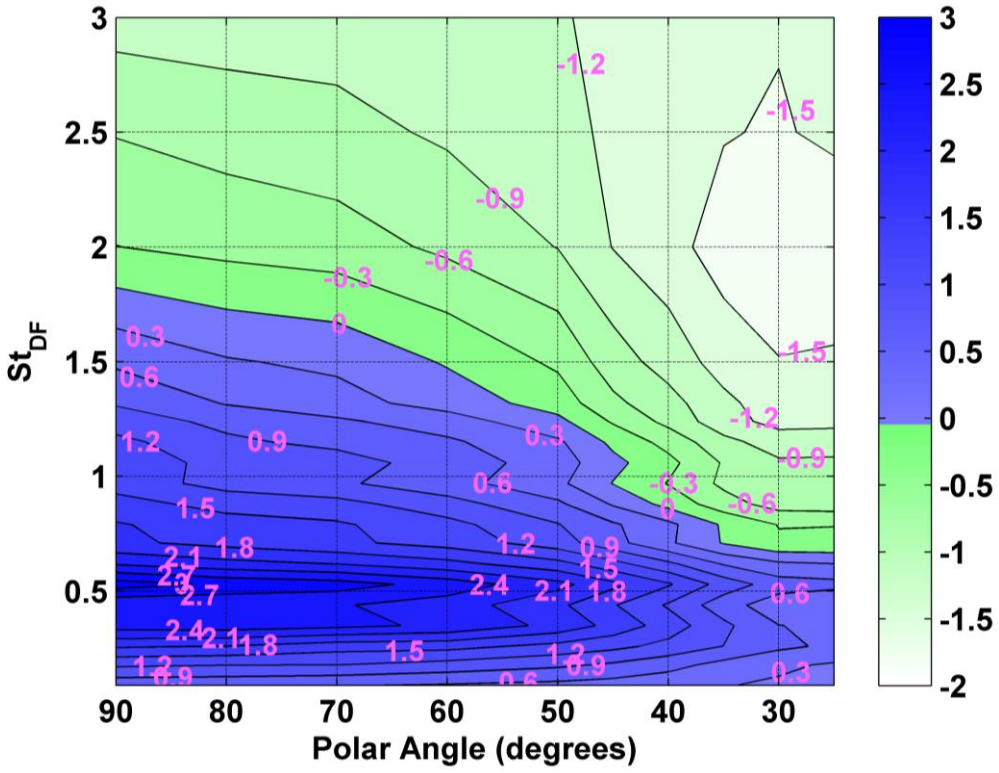

(a)

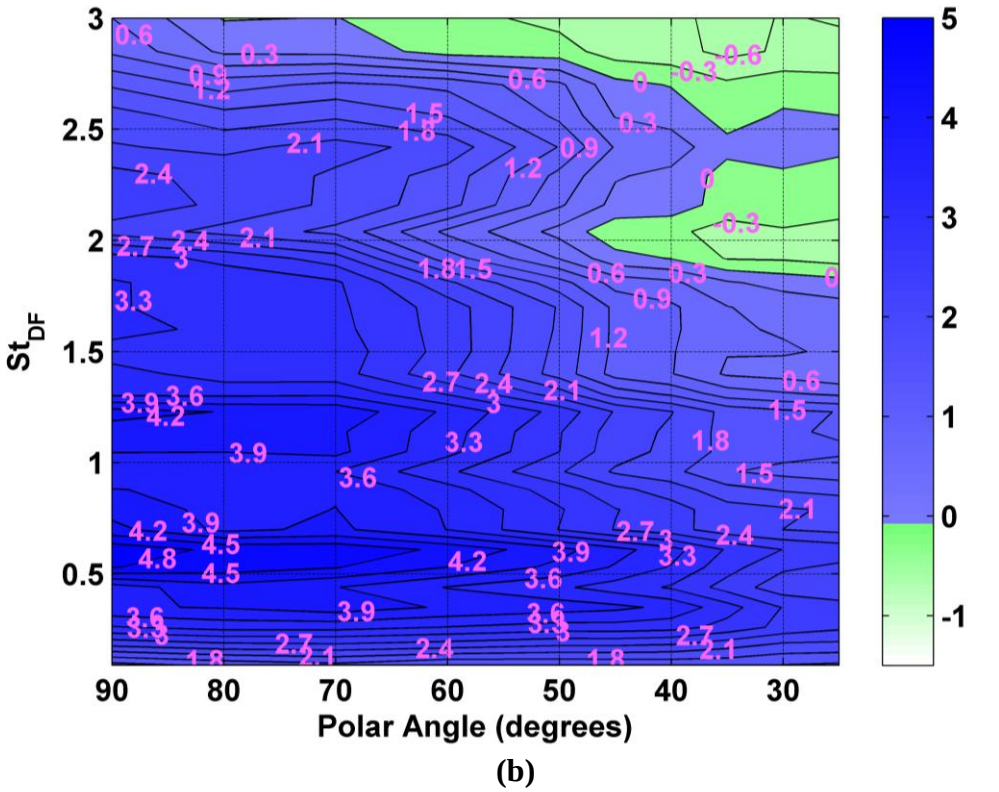

(b)

Figure 4-6: ΔOASPL plots for mode m = 0 (detoned) for (a) an older traditional extension and (b) a new traditional extension showing very different amplification/attenuation rates.

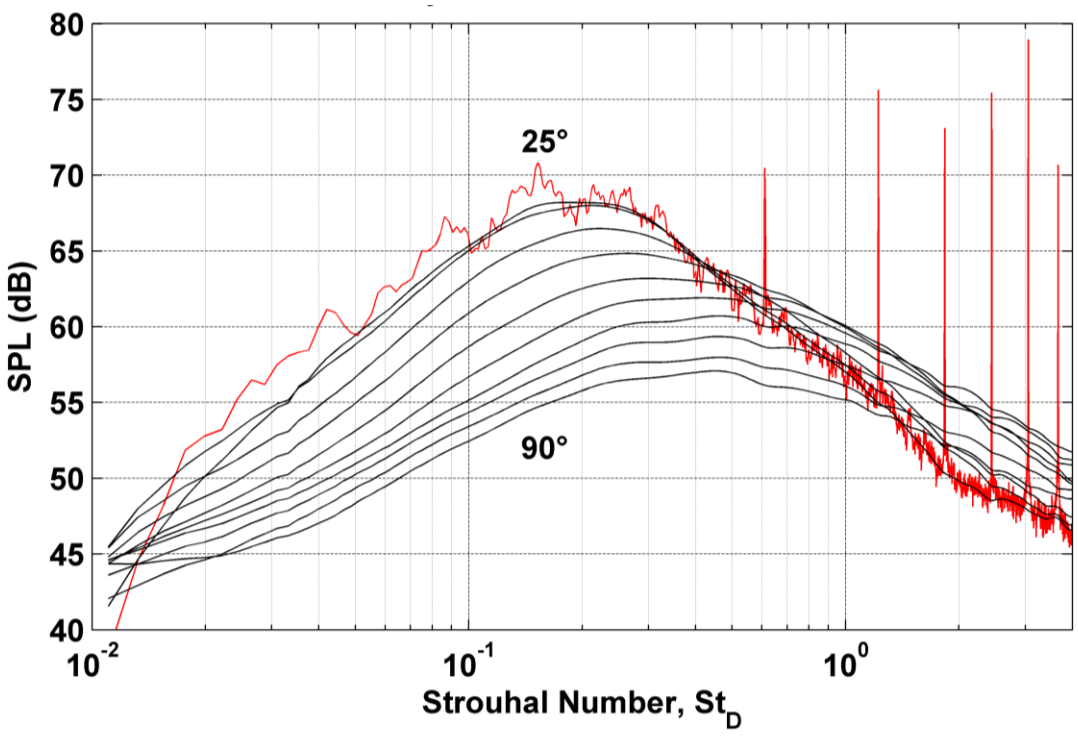

Figure 4-7: Spectra for mode m = 0 and St_{DF} = 0.61 of recaptured data using the new traditional extension. High frequency fluctuations are no longer existent.

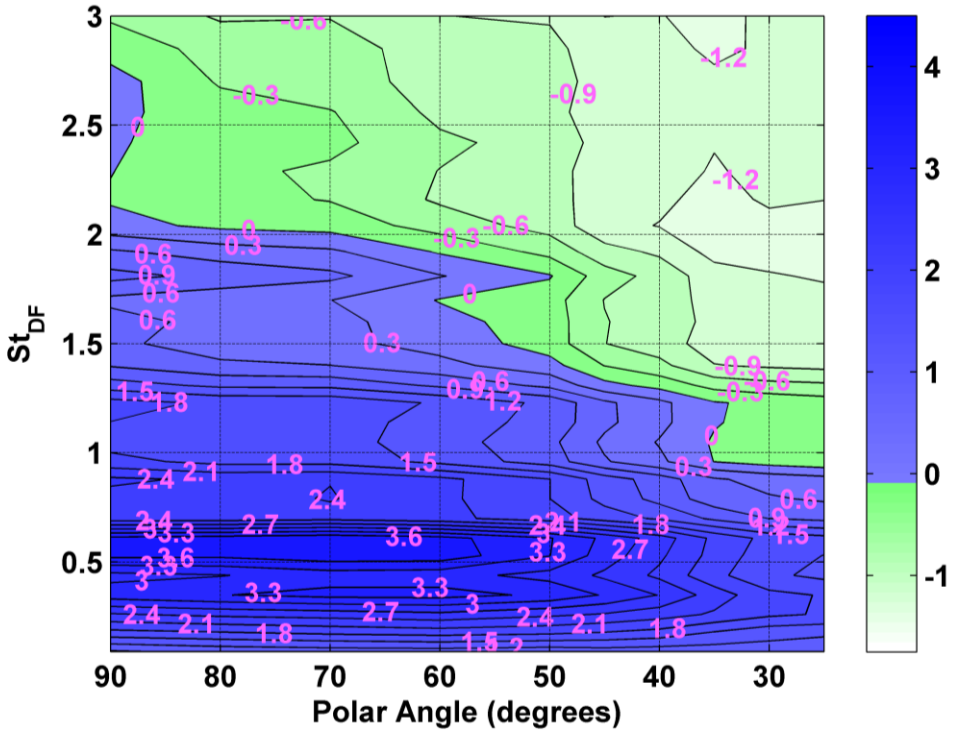

Figure 4-8: ΔOASPL plot for mode m = 0 (detoned) for recaptured data using the new traditional extension. Amplification/attenuation levels are more agreeable with previous research.

4.4. Comparison of Traditional Extension and External Electrode Extension

To compare the effectiveness of the actuators when installed in either the traditional nozzle extension or the external electrode nozzle extension, analysis began with the spectra of both extensions for all forcing frequencies and azimuthal modes. Overall, the general trends and shapes that were realized with the external electrode nozzle extension were consistent with the traditional nozzle extension, yet certain variations between the two do exist.

The first noticeable trend is that the peak values of the forcing tones and their harmonics are reduced in the spectra of the external electrode extension. Figure 4-9 shows the spectra at polar angles of 30° and 90° for the two extensions for a forcing Strouhal number, $St_{DF} = 0.44$ and an azimuthal mode, m = 0. At this combination of forcing parameters, the peaks are on average ~5 dB lower for the external electrode extension. This level of reduction is representative of a good majority of the spectra for other combinations of forcing frequency and azimuthal mode.

A second variation again concerns trends involving forcing tones and their harmonics. When forcing at higher Strouhal numbers ($St_{DF} > 2$) the band of frequencies, centered about the tones, that are greatly elevated above the baseline is much wider and exaggerated for the traditional extension. Figure 4-10 shows the detoned spectra ($St_{DF} = 3.0$, m = 0) for all polar angles as well as the raw, or non-detoned, spectra at 30° as a reference of the forcing tone peak. This figure clearly shows this trend of both the raw spectrum and the detoned spectra of the traditional nozzle extension possessing a noticeable hump around the forcing tone. On the other hand, the spectra for the external electrode nozzle extension, also shown in Figure 4-10, have a much less drastic hump for all angles. This was realized in several other spectra for various modes and high forcing Strouhal number cases.

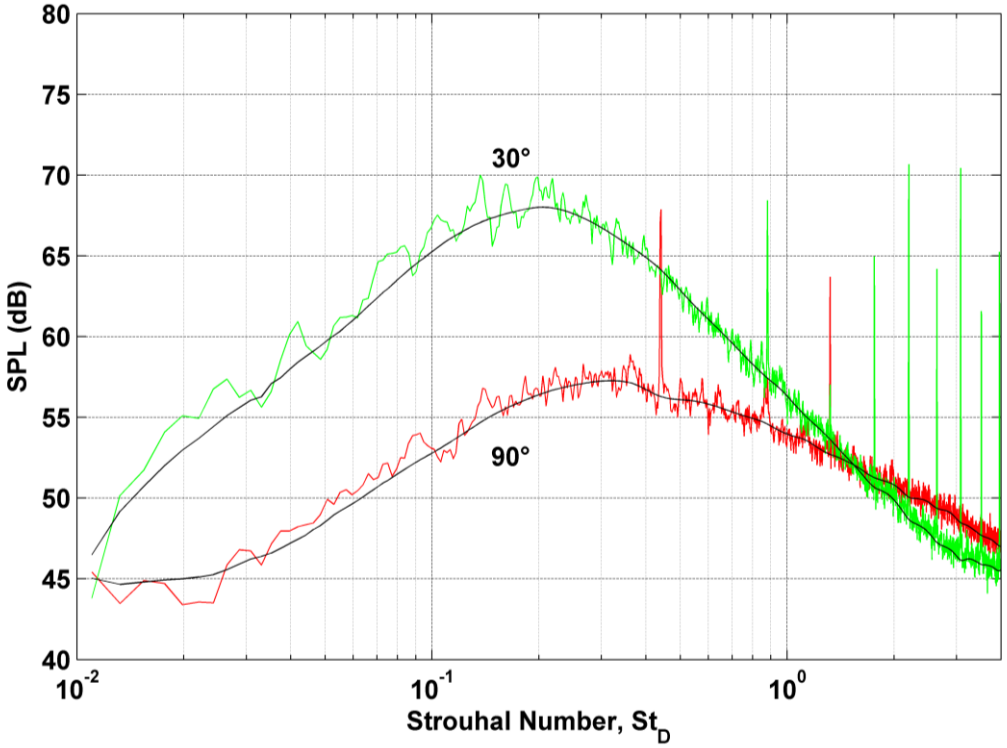

(a)

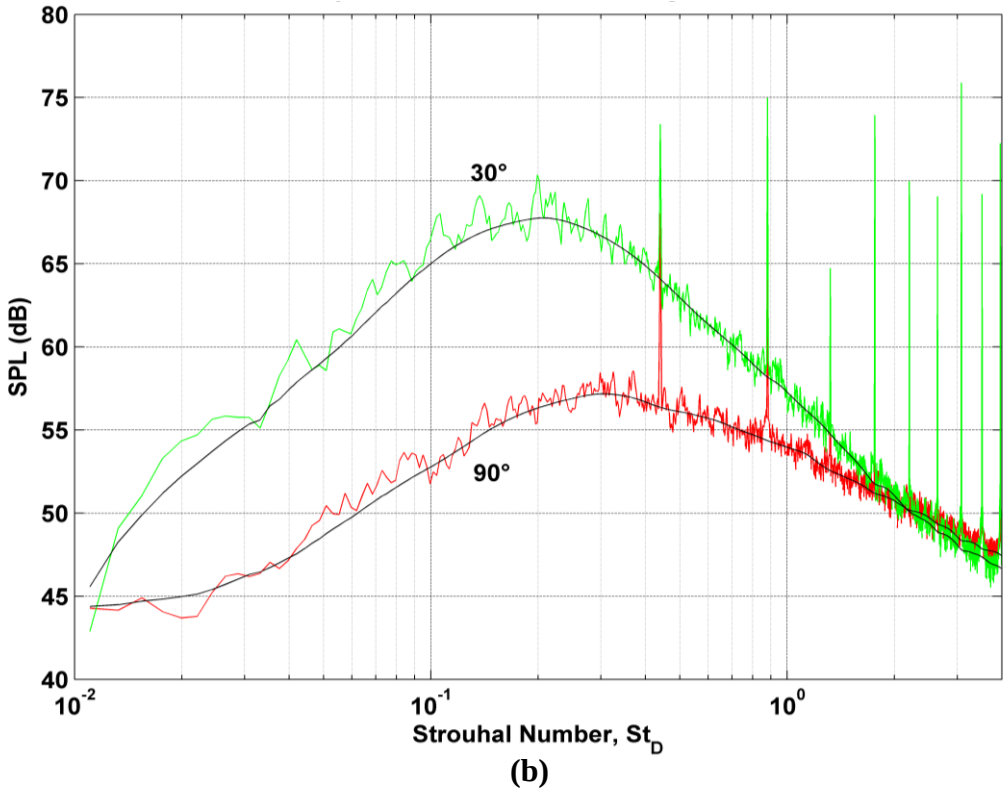

(b)

Figure 4-9: Spectra at 30° and 90° for mode m = 0 and St_{DF} = 0.44 for (a) the external electrode extension and (b) the traditional extension showing differences in forcing tone amplitudes.

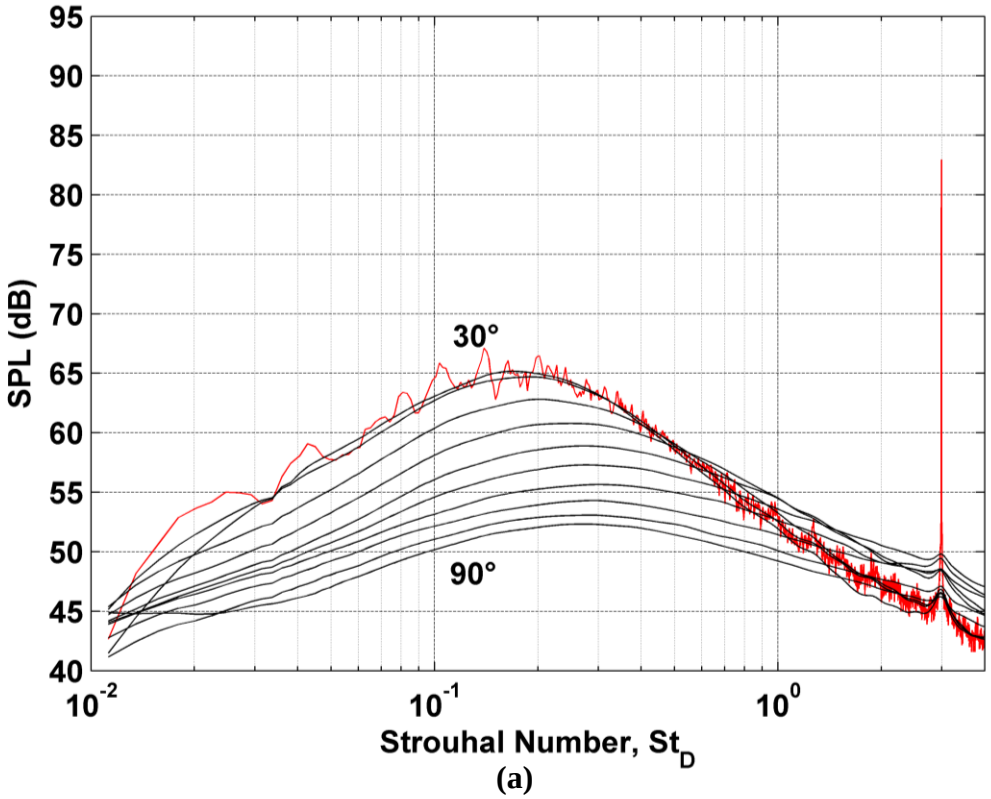

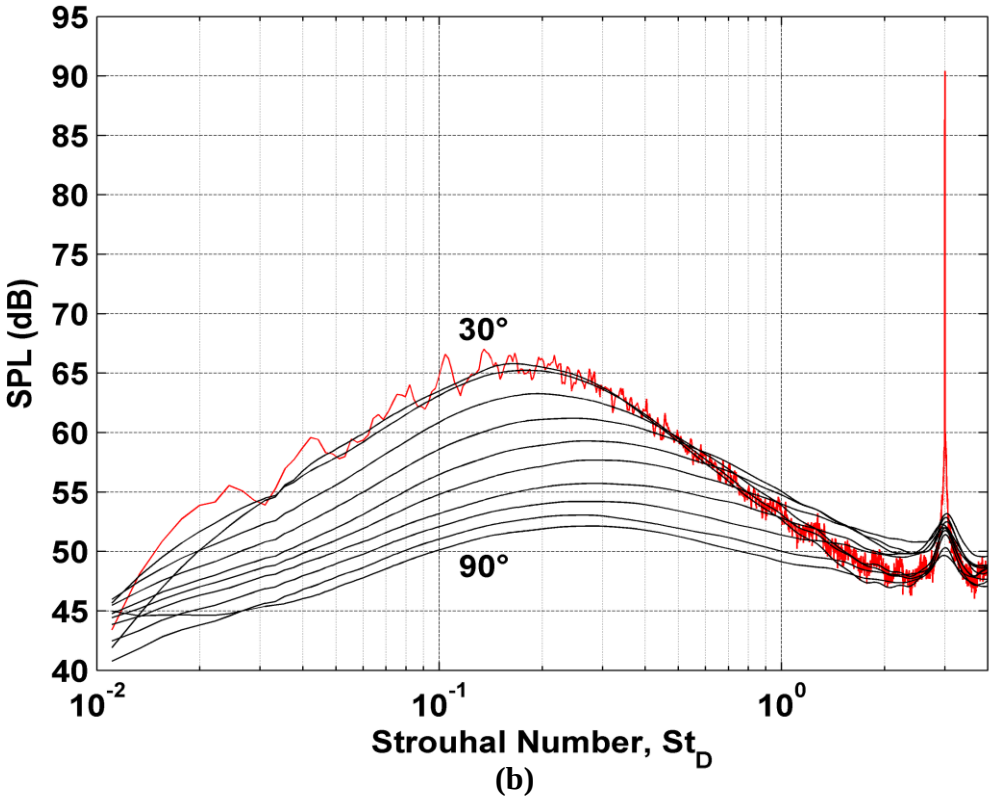

Figure 4-10: Spectra of all polar angles for mode m = 0 and St_{DF} = 3.0 for (a) the external electrode extension and (b) the traditional extension showing differences in response to forcing tones.

Figure 4-10 also shows a third trend occurring in the higher frequency portion of the spectra. As the forcing Strouhal number increases, the high frequency portions of the spectra for the traditional nozzle extension stay at more elevated levels; the spectra do not return to the same rate of decline in SPL of the baseline spectrum and the spectra for the external electrode extension. Figure 4-11 shows this in a more comprehensible manner. The two plots are contours of the SPL changes of the forced spectra over the baseline spectra plotted against forcing Strouhal number on the abscissa and acoustic Strouhal number on the ordinate for a given azimuthal mode, m = 0 at a polar angle of 30°. There are a couple trends portrayed in these plots. First, a red line has been overlaid on both contour maps denoting the collapsed spectra for a forcing Strouhal number, $St_{DF} = 2.5$. These lines show that at high frequencies the SPL levels are indeed more elevated for the traditional nozzle extension. Also, at the lower frequencies for the same forcing Strouhal number, the traditional nozzle extension achieves slightly greater attenuation. Thus, the traditional nozzle extension has greater extremes in comparison to the external electrode nozzle extension.

Figure 4-12 shows two ΔOASPL plots for mode, m = 3—the first for the external electrode nozzle extension and the second for the traditional nozzle extension. It is seen that the amplification and attenuation levels as well as the contour line directions are, in general, similar between the two extensions. Still, there is a variation between these two plots, as well as the ΔOASPL plots for the other azimuthal modes that is worth mentioning. The changeover contour line from amplification to attenuation is slightly more horizontal in the plot for the external electrode nozzle extension; the attenuation levels at smaller polar angles are less while the attenuation levels nearer 90° are greater.

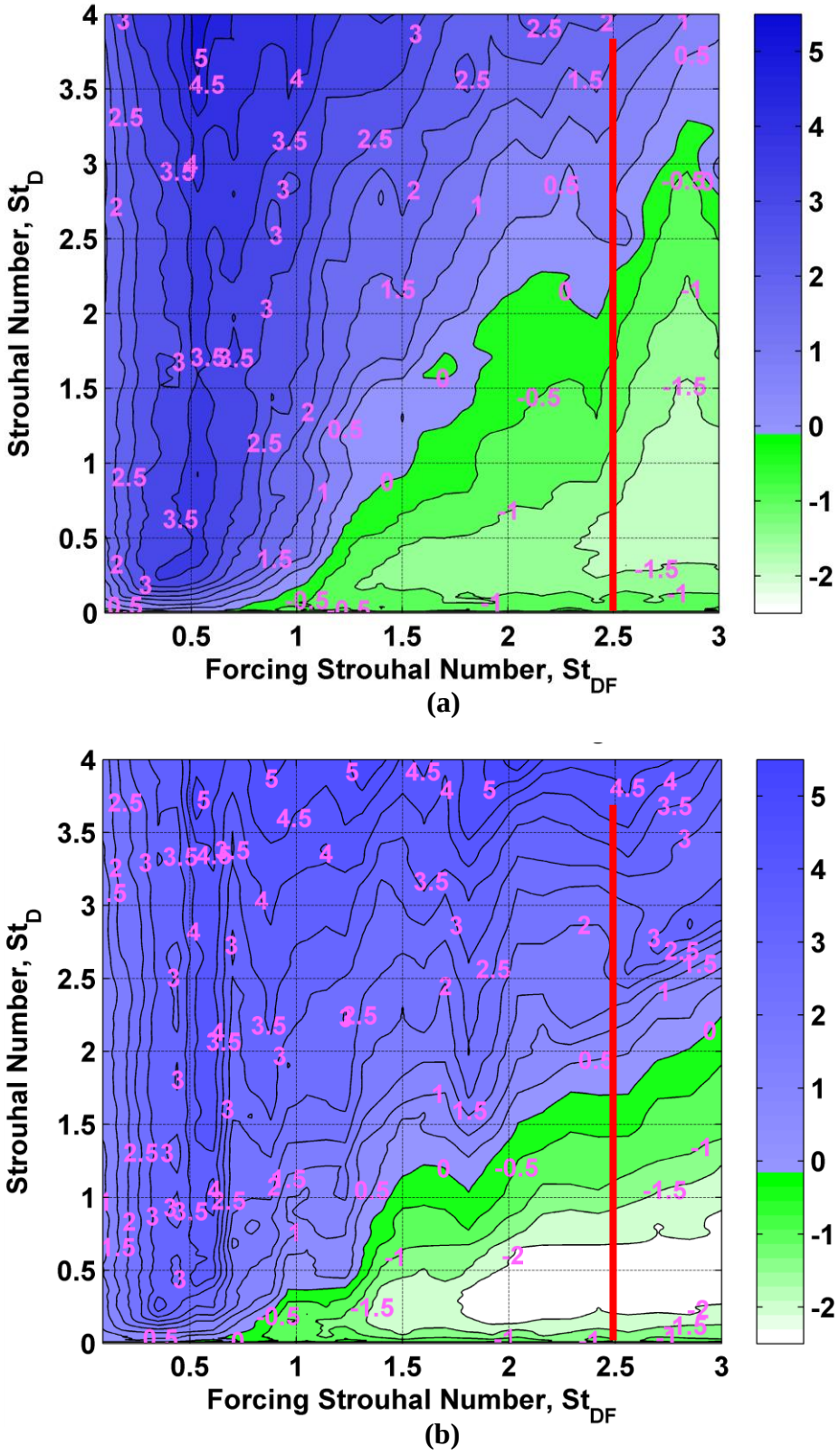

Figure 4-11: ΔSPL (SPL_{forced} - $SPL_{baseline}$) for mode m = 0 @ 30° contour plot for (a) the external electrode extension and (b) the traditional extension.

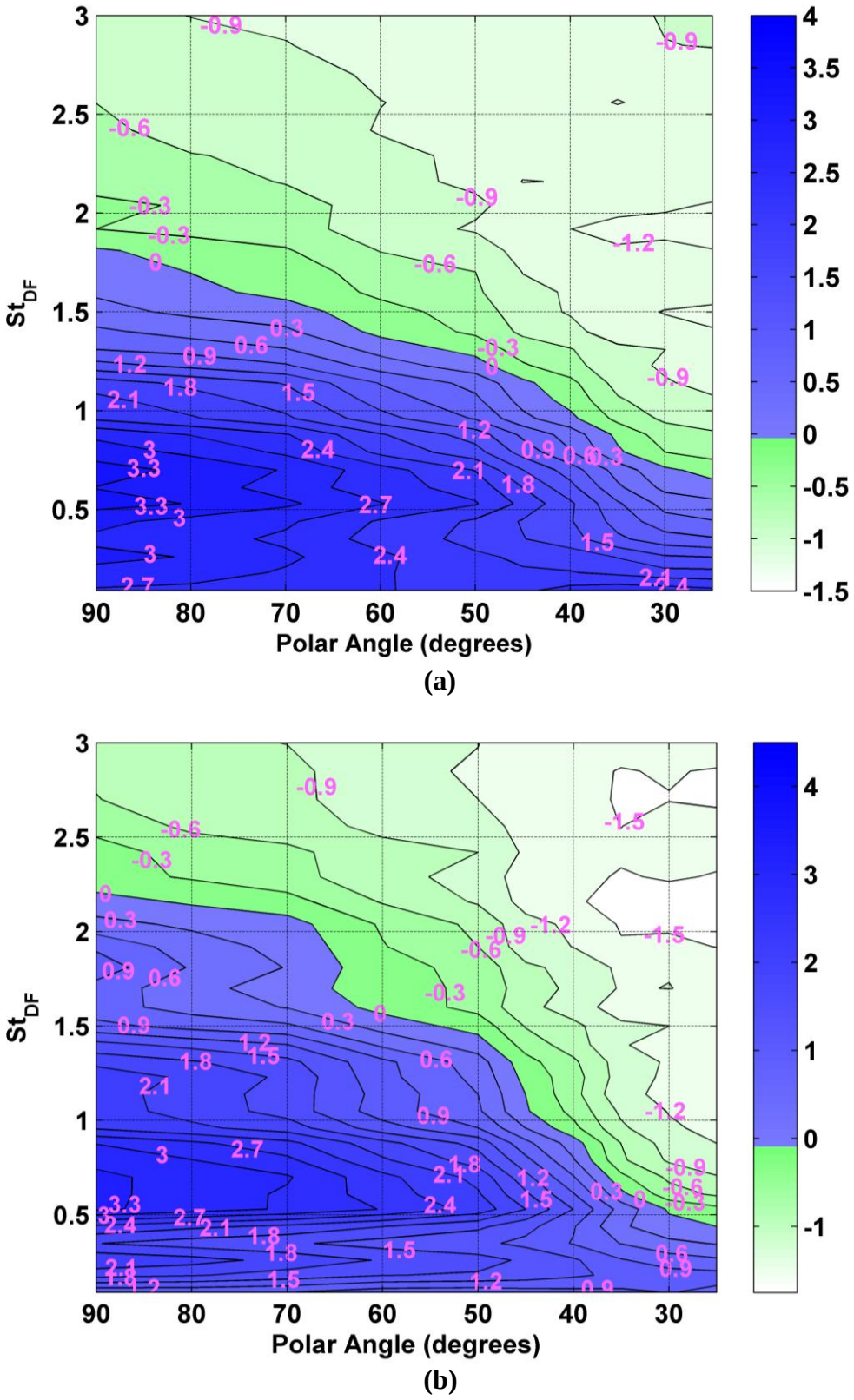

Figure 4-12: ΔOASPL plots for mode m = 3 (detoned) for (a) the external electrode extension and (b) the traditional extension.

Figure 4-13 shows two ΔAAE plots for each nozzle extension. The plots on the left include the spectra in which detoning was not preformed; thus, the contributions from the actuator tones are included. The plots on the right do not include the actuator tones. In comparing a single pair of plots for either extension, it is noticed that detoning has the effect of collapsing and smoothing the plots for all azimuthal modes. Yet, when comparing one pair of plots to the other it can be seen that the smoothing effect when detoning for the traditional nozzle extension is much greater than for the external electrode nozzle extension. The non-detoned plot for the external electrode nozzle extension already has the same general shape that the two detoned plots display. Thus, as pointed out above, the SPL of the forcing tone and its harmonics are lower for the external electrode nozzle extension. It should also be mentioned that for all modes both extensions achieve a similar maximum ΔAAE reduction of ~1 dB.

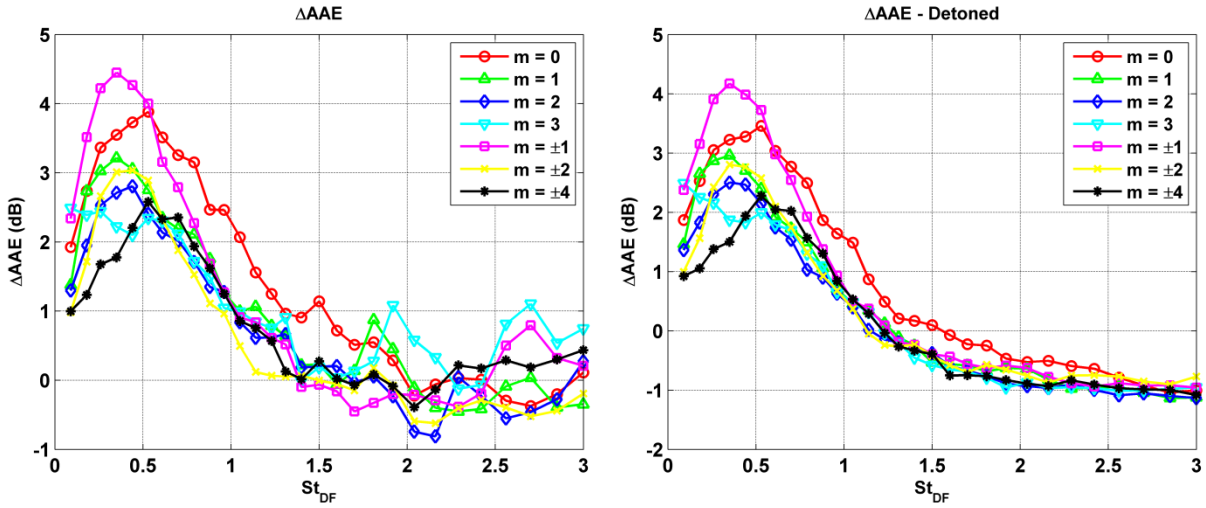

(a)

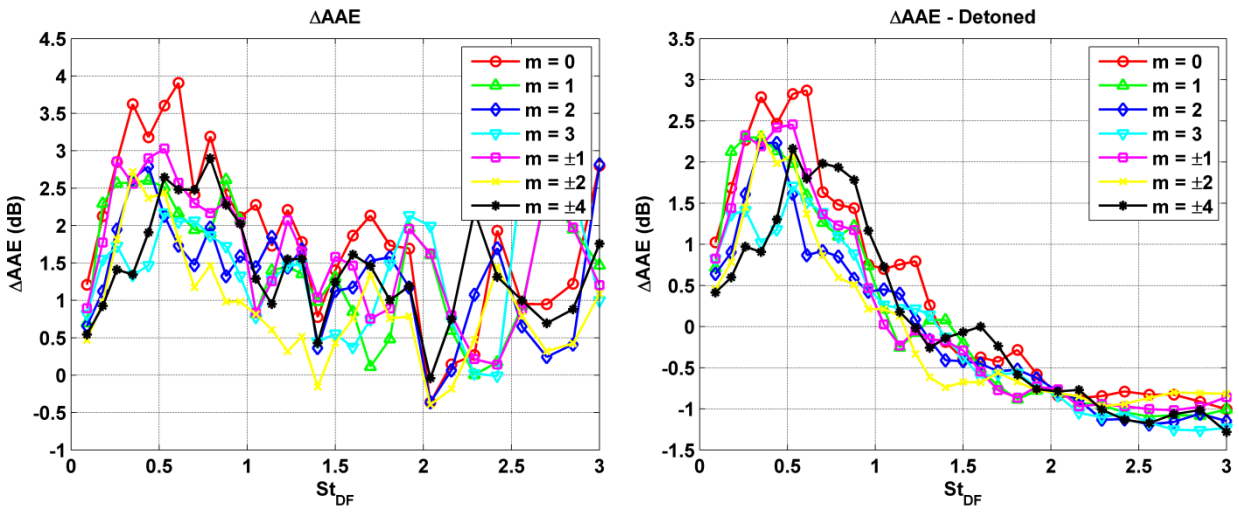

(b)

Figure 4-13: ΔAAE plots, non-detoned and detoned spectra, for (a) the external electrode extension and (b) the traditional extension.

Though the above variations are present between the results of the two nozzle extension designs, the electrodes, when mounted externally, were able to affect the same overall trends; amplification and attenuation were still realized at forcing frequencies, azimuthal modes and polar angles characteristic of the traditional nozzle extension. Thus, it is concluded that fluidic ejection is not the primary mechanism by which the actuators affect the shear layer growth of the jet downstream of the nozzle exit, and that it is instead the direct perturbation by the Joule heating or the resulting pressure waves. Moreover, the magnitudes of amplification and attenuation are on par with that of the traditional nozzle extension, and, therefore, a second conclusion is suggested. With less energetic actuation, the actuators in their new position still have control authority over the jet. Thus, in terms of noise attenuation potential, the actuators in combination with the traditional nozzle extension oversaturate the jet; this implies that actuation power could be reduced while still obtaining the same results when using an optimized setup.

CHAPTER 5: Conclusion and Future Work

Presented in this thesis is a description of the research conducted to study the effect of the plasma shielding ring groove of a traditional nozzle extension on the control authority of the localized arc filament plasma actuators (LAFPAs) developed at the Gas Dynamics and Turbulence Lab at The Ohio State University. It had been suggested that the groove was crucial for actuation beyond simply shielding the plasma from the high-speed jet. In order to investigate this theory a new extension was manufactured that relocated the actuators outside of any cavity.

Background information for the dynamics of jet flows and their noise emission is given as well as a description of the facility and data acquisition instruments used during the experiments. A thorough introduction to the metrics and plots used in analyzing acoustic data is given. Next, the multiple design iterations of the new external electrode nozzle extension are presented with a detailed description of the final, operational design. Then, representative plots of the first data set captured using the newly manufactured traditional nozzle extension show that abnormal behavior is noticed in the mode, m = 0 data. Unsure as to why these trends are noticed, the data was recollected. Sample plots are given verifying that the second set of data is in better agreement with old traditional nozzle extensions and is satisfactory for comparisons to the external electrode nozzle extension.

These comparisons of the acoustic data for both nozzle extensions are used to analyze the effect of the ring groove on the control authority of the LAFPAs. A few variations are noticed between the two sets of data with most of these concerning the actuator tones. Still, the external electrode nozzle extension is capable of producing the same attenuation/amplification trends with similar magnitudes. Therefore, it is discovered that the ring groove is not crucial for proper

control of the jet by the actuators and that fluidic ejection is not the mechanism by which the actuators perturb the instabilities of the jet.

Several aspects of the jet flow experiments conducted generate the need and desire for additional research. First, a study should be performed on the data initially taken with a new extension to determine the reasons for the odd behavior noticed in the spectra and this "break-in" period that has been noticed by several researchers at the GDTL. Second, the effect of electrode spacing on the attenuation/amplification results of the actuators should be studied in order to better quantify the comparative results for both types of nozzle extensions (recall that the traditional nozzle extension has an electrode spacing of 4 mm while the final external electrode extension has a spacing of 3.5 mm). Third, results when troubleshooting the stability of the plasma of the external electrode nozzle extension suggest that a similar nozzle extension originally designed with an electrode spacing of 3.5 mm and no recess on the face would be capable of producing stable plasma; this would remove any concerns, as small as they may be, regarding the dynamics of the recess during actuation. And last, though one more suggested mechanism has been rejected, the exact physics of the actuator control authority always needs further research.

REFERENCES

[1] Samimy, M., Zaman, K.B.M.Q., and Reeder, M.F., "Effect of Tabs on the Flow and Noise Field of an Axisymmetric Jet", *AIAA Journal* Vol. 31, No. 4, 1993, pp. 609-619.

[2] Kearney-Fischer, M., Kim, J.H., and Samimy, M., "Noise Control of a High Reynolds Number Mach 0.9 Heated Jet Using Plasma Actuators", AIAA Paper 2009-3188, 2009.

[3] Paur, J., "The Innovative 787 Carries Being, And Aviation, Ahead", *Wired*, 3 Dec. 2009. Web. 16 Apr. 2010 <http://www.wired.com/autopia/2009/12/boeing-787-dreamliner/>.

[4] Kibens, V., "Discrete Noise Spectrum Generated by an Acoustically Excited Jet", *AIAA Journal* Vol. 18, No. 4, 1980, pp. 434-441.

[5] Zaman, K.B.M.Q., "Jet noise reduction by microjets – a parametric study", AIAA Paper 2009-3129, 2009.

[6] Samimy, M., Kim, J.H., Kastner, J., Adamovich, I., and Utkin, Y., "Active Control of a Mach 0.9 Jet for Noise Mitigation Using Plasma Actuators", *AIAA Journal* Vol. 45, No. 4, 2007, pp. 890-901.

[7] Samimy, M., Kim, J.H., Kastner, J., Adamovich, I., and Utkin, Y., "Active Control of High-Speed and High-Reynolds-Number Jets Using Plasma Actuators", *J. Fluid Mech.* Vol. 578, No. 1, 2007, pp. 305-330.

[8] Kleinman, R.R., Bodony, D.J., and Freund, J.B., "Numerical Modeling of Plasma Actuators in High Speed Jets", AIAA Paper 2009-3190, 2009.

[9] Michalke, A., "On Spatially Growing Disturbances in an Inviscid Shear Layer", *J. Fluid Mech.* Vol. 23, No. 3, 1965, pp. 521-544.

[10] Zaman, K.B.M.Q., and Hussain, A.K.M.F., "Turbulence Suppression in Free Shear Flows by Controlled Excitation", *J. Fluid Mech.* Vol. 103, 1981, pp. 133-159.

[11] Ho, C.-M., and Huerre, P., "Perturbed free shear layers", *Annu. Rev. Fluid Mech.* Vol. 16, 1984, pp. 365-424.

[12] Moore, C.J., "The role of shear-layer instability waves in jet exhaust noise", *J. Fluid Mech.* Vol. 80, No. 2, 1977, pp. 321-367.

[13] Crow, S.C., and Champagne, F.H., "Orderly Structure in Jet Turbulences", *J. Fluid Mech.* Vol. 48, No. 3, 1971, pp. 547-591.

[14] Cohen, J., and Wygnanski, I., "The evolution of instabilities in the axisymmetric jet. Part 1 the linear growth of disturbances near nozzle", *J. Fluid Mech.* Vol. 176, 1987, pp. 191-219.

[15] Morrison, G.L., and McLaughlin, D.K., "Noise Generation by Instabilities in Low Reynolds Number Supersonic Jets", *J. Sound & Vib.* Vol. 65, No. 2, 1979, pp. 177-191.

[16] Hileman, J., and Samimy, M., "Turbulence Structures and the Acoustic Far Field of a Mach 1.3 Jet", *AIAA Journal* Vol. 39, No. 9, 2001, pp. 1716-1727.

[17] Samimy, M. et al., "Flow and Noise Control in High Speed and High Reynolds Number Jets Using Plasma Actuators", AIAA Paper 2846, 2006.